

Photoproduction of $K^+ \Lambda(1520)$ at the BGOOD-Experiment

Emil Otis Rosanowski

Bachelorarbeit in Physik
angefertigt im Physikalischen Institut

vorgelegt der
Mathematisch-Naturwissenschaftlichen Fakultät
der
Rheinischen Friedrich-Wilhelms-Universität
Bonn

Februar 2023

Ich versichere, dass ich diese Arbeit selbstständig verfasst und keine anderen als die angegebenen Quellen und Hilfsmittel benutzt sowie die Zitate kenntlich gemacht habe.

Bonn,
Datum

.....
Unterschrift

- 1. Gutachter: Prof. Dr. Hartmut Schmieden
- 2. Gutachter: Prof. Dr. Klaus Desch

Acknowledgements

I would like to thank Professor Dr. Hartmut Schmieden for making this bachelor thesis possible. Additionally I would also like to thank Dr. Tom C. Jude and Dr. Katrin Kohl as well as the rest of the people involved with *BGOOD* for the support and help during my work. Finally I want to thank Professor Dr. Klaus Desch for acting as second referee.

Contents

1	Introduction	1
2	Physical context	2
2.1	The Standard Model of particle physics	2
2.1.1	Properties of the $\Lambda(1520)$	2
3	Experimental setup and analysis tools	4
3.1	Setup of the <i>BGOOD</i> -experiment and <i>ELSA</i>	4
3.1.1	<i>ELSA</i>	5
3.1.2	Photon Tagger	6
3.1.3	Central detector	7
3.1.4	Forward spectrometer	8
3.1.5	Photon flux measuring detectors	9
3.2	Analysis tools	9
3.2.1	Simulation of data	9
3.2.2	Often used physical relations	10
3.2.3	Cross section	11
4	Particle selection	13
4.1	Resolution of particles in the forward spectrometer	14
4.2	Resolution of π^0 in the <i>BGO Rugby Ball</i>	15
5	Determination of the differential cross section of the reaction $\gamma p \rightarrow K^+ \Lambda(1520)$	17
5.1	Identification of decays with charged particles	17
5.1.1	$K^+ \Lambda(1520) \rightarrow K^+ p K^-$	17
5.1.2	$K^+ \Lambda(1520) \rightarrow K^+ \Sigma^+ \pi^-$	19
5.2	Inclusive identification of $K^+ \Lambda(1520)$	20
5.2.1	Requirements for the identificaton of $K^+ \Lambda(1520)$	20
5.2.2	Properties of the different requirements	20
5.2.3	Reconstruction Efficiency	25
5.2.4	Determination of the cross section of $\gamma p \rightarrow K^+ \Lambda(1520)$	25
5.2.5	Estimation of the systematic errors	29
6	Summary and outlook	31

A Appendix	32
A.1 Fits to the missing mass	33
Bibliography	36
List of Figures	38
List of Tables	40

Introduction

This work discusses the photoproduction of the $\Lambda(1520)$ in the reaction $\gamma p \rightarrow K^+ \Lambda(1520)$. It is an exploratory study for the *BGOOD* experiment. This particle is especially of interest due to the $\Lambda(1405)$, which is its spin partner. The $\Lambda(1405)$ has a smaller mass than the $N^*(1535)$ even though it contains an *s*-Quark instead of a *d*-Quark [1]. It has $J^P = 1/2^-$ and the $\Lambda(1520)$ has $J^P = 3/2^-$ [1]. Interestingly the mass difference between the two particles is greater than it is between the analogous particles in the nucleon sector, which are the $N^*(1535)$ and the $N^*(1520)$. As a result of this and further studies, the $\Lambda(1405)$ is believed to be a hadronic molecule [2].

If the $\Lambda(1405)$ is not a classical three-quark state anymore, it poses the question whether its spin partner, the $\Lambda(1520)$, even is one. Therefore the particle has become of interest itself. The setup of the *BGOOD* experiment at the electron accelerator *ELSA* in Bonn is ideal for this analysis since production of hadronic molecules is supposed to be much stronger at low momentum transfer and therefore at forward K^+ angles. The forward spectrometer at *BGOOD* allows angles down to 1.5° [3]. Thus angles can be reached which have shown interesting effects in earlier experiments (*LEPS* [4]).

The goal of this work is to study whether the $\Lambda(1520)$ can be reconstructed with the experimental setup of *BGOOD*. If this is possible, a more precise analysis can be performed in the future.

Physical context

2.1 The Standard Model of particle physics

The Standard Model of particle physics is a theory that includes complex mathematical models like quantum chromodynamics which describes the interaction of particles with colour charge. The matter is made up of leptons and quarks, latter of which form the hadrons. Former include up, down, strange, charm, top and bottom quarks, that all have spin $s = \frac{1}{2}$ and have either charge $q = \frac{2}{3}$ or $q = -\frac{1}{3}$ of the elementary charge [5, p. 205]. As the leptons are not important for this work, they will not be discussed here but are shown in figure 2.1 alongside the other particles. The particles forming the matter all have corresponding anti-particles which are not shown in the figure. Nonetheless the Standard Model cannot explain all observations and still has a multitude of free parameters, which have to be determined experimentally [5, p. 208].

Hadrons can have several different configurations to fulfil conditions required by the quantum numbers. The quark model proposed by GELL-MANN allows for the construction of baryons from three quarks and mesons from one quark and one anti-quark [6]. Moreover more configurations like a hadron made of six quarks or four quarks and one anti-quark are possible [6]. All hadrons that are not built from two or three quarks are called exotic hadrons. Many experiments try to find these exotic hadrons and some have found them (e.g. LHCb [7]).

Another way to build a particle of five quarks would be as a hadronic molecule. These are shallowly bound hadrons (a precise definition is given for example by GUO ET AL. [2]). The $\Lambda(1405)$ seems to be such a hadronic molecule as described above [2]. Its spin partner, the $\Lambda(1520)$, is therefore also a possible candidate to be a hadronic molecule (e.g. T. HYODO ET AL. investigated the theoretical consequences, if the $\Lambda(1520)$ was a molecule [8]).

2.1.1 Properties of the $\Lambda(1520)$

The PDG [1] states a mass of $m_{\Lambda(1520)} \approx 1519 \text{ MeV}$ and width of $\Gamma_{\Lambda(1520)} \approx 16 \text{ MeV}$ for the $\Lambda(1520)$. It has strangeness $S = -1$ and spin $J^P = 3/2^-$ [1]. With a branching ratio of $\Gamma_i/\Gamma = (45 \pm 1) \%$ it decays into $N\bar{K}$ [1]. The decay into $\Sigma\pi$ has a branching ratio of $\Gamma_i/\Gamma = (42 \pm 1) \%$ [1]. Lastly the decay channel into $\pi\pi\Lambda$ shows a branching ratio of $\Gamma_i/\Gamma = (10 \pm 1) \%$ [1]. Figure 2.2 shows the different decay channels.

Standard Model of Elementary Particles

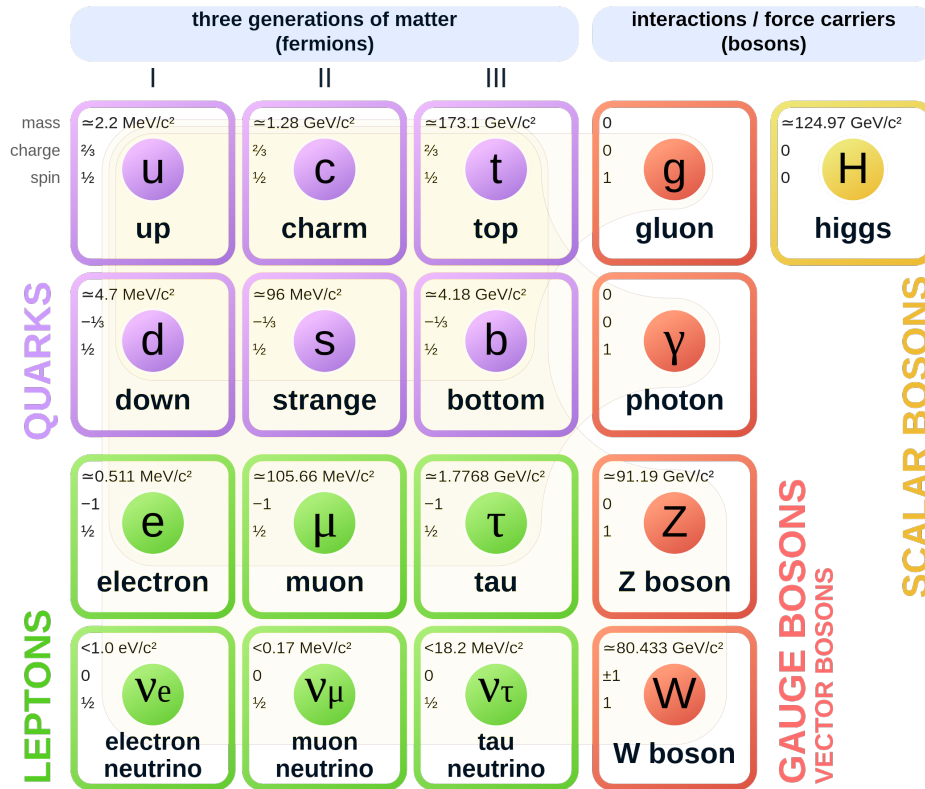


Figure 2.1: Particles in the Standard Model of physics [9].

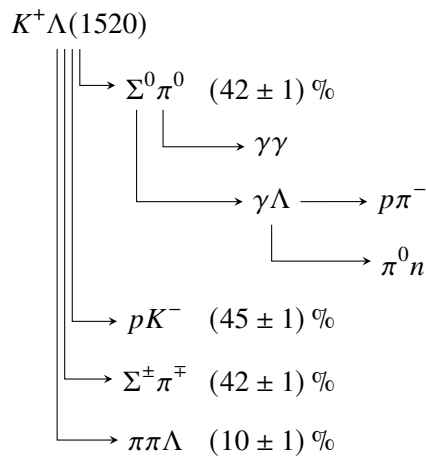


Figure 2.2: Decay scheme of the $\Lambda(1520)$. The decay channels with small branching ratios are left out. As the PDG does not state specific branching ratios for the different charges, all $\Sigma\pi$ -channels have the same value, which is the branching ratio for all three possibilities together. The branching ratios are taken from [1].

Experimental setup and analysis tools

3.1 Setup of the *BGOOD*-experiment and *ELSA*

The experiment is located at the *ELSA* accelerator in Bonn. Figure 3.1 and 3.2 show an overview of the experiment. The setup consists of many smaller detectors, which can be divided into a central part and a forward part. The presented information is from the technical paper of *BGOOD* [3].

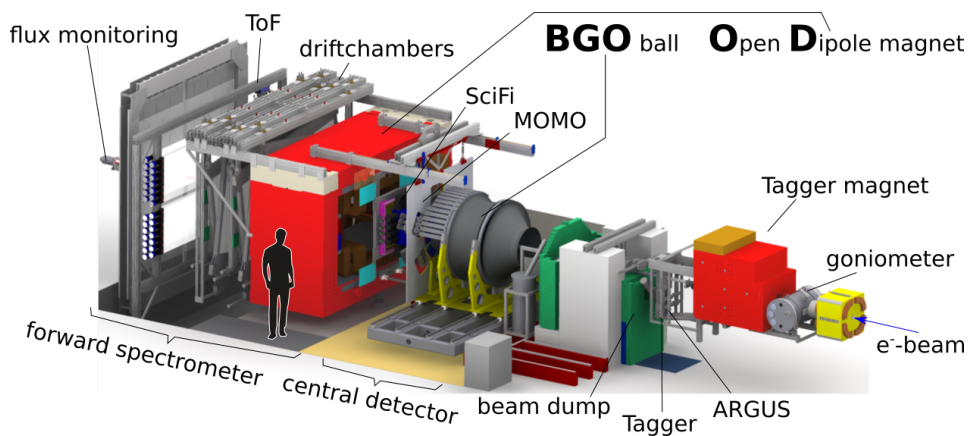


Figure 3.1: A three dimensional view on the *BGOOD* experiment. Picture taken from [3].

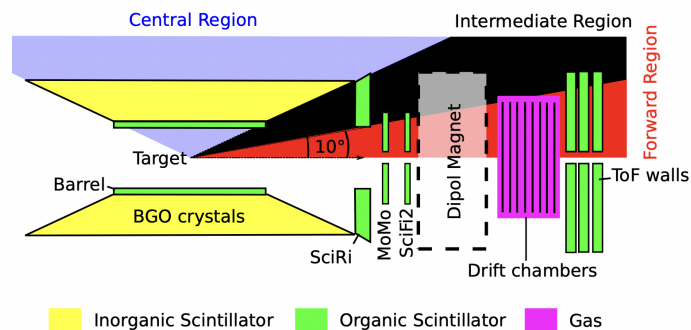


Figure 3.2: Overview of all detectors. The different detection mechanisms are coloured. The illustration does not scale. The figure was taken from the PhD thesis of Georg Scheluchin [10, p. 17]

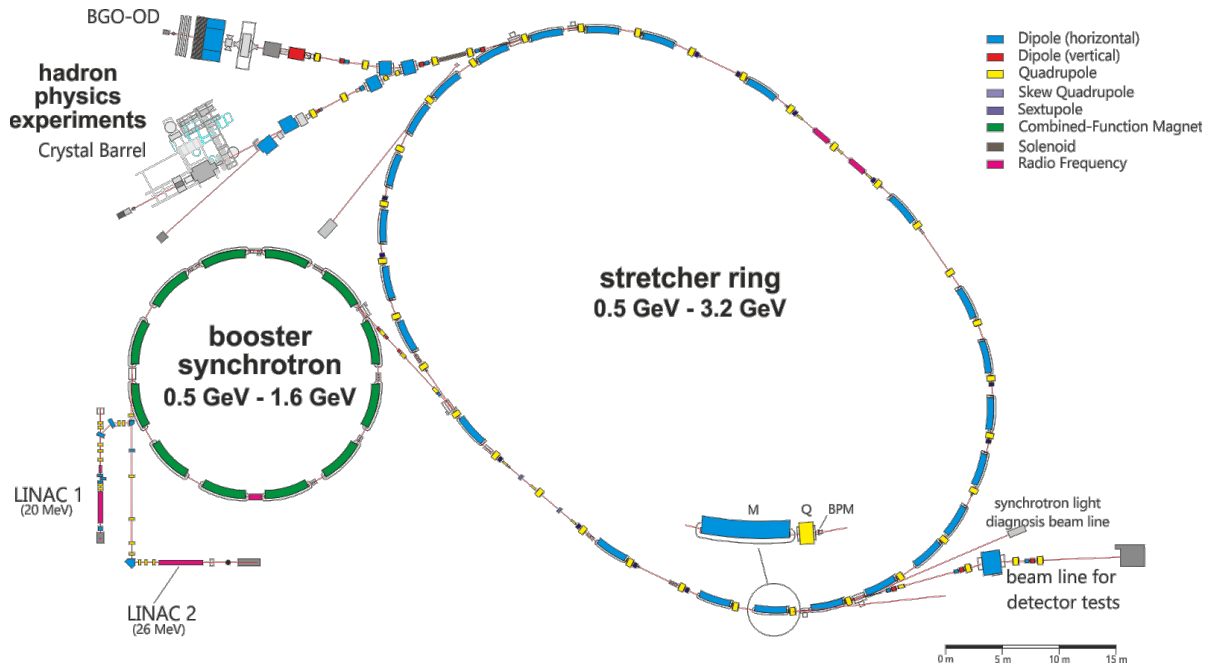
3.1.1 ELSA

Further information can be looked up in the technical paper or in [11] and [12]. The high energy electrons are provided by the electron accelerator *ELSA* (**E**lectron **S**tretcher **A**ccelerator). It consists of three parts, which are shown in figure 3.3. In a first step the electrons are boosted to up to 26 MeV in the linear accelerator *LINAC2*. Afterwards the electrons are inserted into the booster synchrotron. Here the electrons can reach energies between 0.5 GeV and 1.6 GeV. The last step is the stretcher ring, which accelerates the electrons up to 3.2 GeV.

The important function of this last part is not mainly the acceleration but the stretching of the electron pulse. This enables an almost continuous current, which is needed for the experiments.

Apart from the main experiments *Crystal Barrel* and *BGOOD* the electron beam is also used for detector tests.

The synchrotron has a circumference of 69.9 m, while the stretcher ring has a circumference of 164.4 m.

Figure 3.3: Setup of *ELSA*. Figure taken from [13].

3.1.2 Photon Tagger

As this experiment focuses on photoproduction, photons have to be produced from the electrons and their energy has to be determined. For this purpose, the high energy electrons hit a radiator (for example a diamond) and undergo bremsstrahlung, which produces photons. The diamond radiator (thickness $500\ \mu\text{m}$ [10]) is able to produce linearly polarised photons from coherent bremsstrahlung while copper radiators of different thickness can be used for unpolarised photons. However the polarisation will not be important in this work. Since bremsstrahlung produces a continuous energy spectrum, the photon energy needs to be determined in order to understand the reaction fully. To determine the photon energy the tagger is used whose working principle is shown in figure 3.4. It consists of a dipole magnet and a hodoscope. The dipole magnet forces the electrons trajectory to curve in the magnetic field depending on their momentum. Therefore the energy E' of the post-bremsstrahlung electrons can be calculated from the position at which they hit the hodoscope. Now the energy E_γ of the photons is also known as it is the difference between the electron beam energy and the post bremsstrahlung electron. The post bremsstrahlung electrons as well as the electrons, which have not undergone bremsstrahlung end up in the beam dump. This way only the photons reach the target in the central part of the experiment. Another important part of the tagger is the high time resolution as the signal from it is used as a start time for all triggers and detectors. Therefore it is especially important for time of flight measurements.

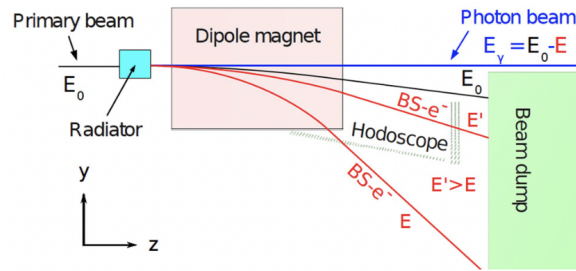


Figure 3.4: Schematic setup of the photon tagger. Figure taken from [3, p. 12]

3.1.3 Central detector

The main part of the central detector is the *BGO*-calorimeter. It has the shape of a rugby ball and is therefore often referred to as *BGO Rugby Ball*. It encloses the target itself and covers a polar angle from 25° to 155° . Thus only the forward and backward direction are not covered. The name of the detector derives from the material, which is bismuth germanate (abbreviated as *BGO*). The detector consists of 480 crystals which are divided in 15 sections of 32 crystals each. Photomultipliers are connected to the crystals to read out the scintillation light yield. The resulting signal is processed by analogue-digital-converters (ADC), which achieve a time resolution of 2 ns.

Additionally a scintillator barrel is placed inside the rugby ball, which is 43 cm long and has a mean radius of 9.75 cm. It is made up of 32 scintillator parts of BC448 (Saint-Gobain). This detector is used to distinguish charged and neutral particles. Separating particles by charge is possible since the detection efficiency is $\approx 98\%$ for charged and just $< 1\%$ for neutral particles. Inside the barrel two *MWPC*s (Multi Wire Proportional Chamber) are placed. These are gas detectors for track reconstruction, but were not used in this thesis [10].

The gap between the central detector and the forward spectrometer is covered by *SciRi* (Scintillating Ring detector), which provides information about the direction of charged particles. In the future this gap will be covered by a multi-resistive plate chamber (*MRPC*) with excellent time and momentum resolution. In this thesis only the central detector and the forward spectrometer were used.

Figure 3.5 shows a side view of the *BGO Rugby Ball*.

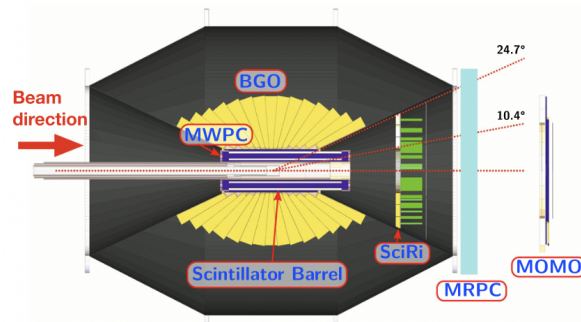


Figure 3.5: Side view of the *BGO Rugby Ball*. Figure taken from [3, p. 6].

3.1.4 Forward spectrometer

The spectrometer in forward directions covers polar angles from approximately 12° down to 1.5° . The main part is the open dipole magnet, which gives the experiment the second half of its name (BGO Open Dipole). The detectors of the forward spectrometer are *MOMO*, *SciFi2*, the drift chambers and *ToF*. The momentum is obtained by measuring the tracks in front of and behind the magnet, while the time of flight is measured by *ToF* which gives β (velocity as $c = 1$ in this work). This information is used to calculate the mass of the particles.

Behind these detectors the photon flux is measured with *GIM* and *FluMo*, which are not part of the forward spectrometer.

MOMO* and *SciFi2

These detectors determine the position of charged particles before they enter the field of the dipole magnet which is placed behind *MOMO* and *SciFi2*. The detector *MOMO* is made out of 672 scintillating fibres which are arranged in three layers that are tilted by 60° respectively. The three layers are needed in case two particles hit *MOMO* at the same time which would result in four possible positions for the two particles if only two layers are used. Additionally the detector *SciFi2* is used, which consists of only two layers and a total of 640 scintillating fibres. It covers an area of $66 \times 51 \text{ cm}^2$. Combining both detectors an azimuthal angle down to 1.5° is covered.

Dipole magnet

The dipole magnet is the main part of the forward spectrometer. Magnetic fields up to 0.4 T can be produced [10]. Charged particles travelling through this field have a curved trajectory due to the Lorentz force, the radius of which depends on their momentum which can therefore be determined. The trajectory is measured using the tracking detectors in front of and behind the magnet.

Drift chambers

Behind the dipole magnet the drift chambers are placed. There are eight drift chambers which are arranged vertically, horizontally and tilted by $\pm 9^\circ$. Altogether an active area of $246 \times 123 \text{ cm}^2$ is covered. The purpose of these detectors is the tracing of particles and precise measurement of their position. The schematic construction of the double layered drift chambers is shown in figure 3.6.

The wires have a diameter of $25 \mu\text{m}$ and are made out of tungsten. As the strong photon beam in the centre would lead to unwanted signals and high dead times, the wires have a diameter of $100 \mu\text{m}$ in an area of $5 \times 5 \text{ cm}^2$ around the centre. This reduces the electric field and therefore only few events surpass the threshold in this area. The used mixture of gas consists of 70 % argon and 30 % CO_2 , which helps to reduce the dead time.

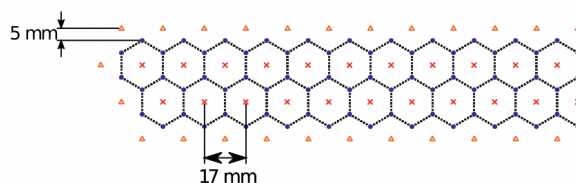


Figure 3.6: Construction of a drift chamber. Figure taken from [14, p. 27]

ToF

The *ToF*-walls (**T**ime-**o**f-**F**light) make up the last part of the forward spectrometer. Scintillators are used to measure the charged particles 5.6 m away from the target. In total an area of $3 \times 3 \text{ m}^2$ is covered by three walls which are themselves split up into bars. This detector measures the time of flight for the β and position. As with the detectors before a hole in the centre exists to let the photon beam as well as produced e^+e^- -pairs through. The photons are measured by the detectors behind.

3.1.5 Photon flux measuring detectors

The photon flux is measured behind the forward spectrometer by the detectors *GIM* and *FluMo*. *GIM* (**G**amma **I**ntensity **M**onitor) is a lead glass detector which absorbs fully but is susceptible to radiation damage. Hence it is only placed in the beam at low intensities for calibration purposes and is moved out of the beam for the data acquisition. At this point *FluMo* (**F**lux **m**onitor) which is a detector made out of five plastic scintillators takes over. It is calibrated with the help of *GIM* but is more resistant to radiation and can be used with the full beam. The calibration is needed for *FluMo* only detects a fraction of the photons detected by *GIM*.

3.2 Analysis tools

The analysis carried out in this work uses the framework ExPIORA¹. ExPIORA was originally developed for the *Crystal Barrel* experiment but was adapted for the *BGOOD* experiment in 2011 [14, p. 126]. The underlying structure is taken from Root. The analysis framework Root is based on C++ but can also be used in python [15]. A big advantage of Root is the speed of the analysis and the storage of data as well as the implementation of certain physics specific classes like four-vectors (see 3.2.2).

3.2.1 Simulation of data

To determine the reconstruction efficiency Monte-Carlo simulated data is used. The whole experimental setup of *BGOOD* is implemented in the framework of ExPIORA. The reaction particles are generated, which in the case of this work are a photon from the radiator and a proton at rest as initial particles and a K^+ and $\Lambda(1520)$ as final state particles. The decay of the final state particles, their tracks and interactions are simulated using Geant4². Further information on Geant4 can be found in [16]. If a certain threshold in energy is achieved, a detector hit is created. Afterwards the processing of the data is identical to real

¹ Extended **P**luggable **O**bjectoriented **R**oot **A**nalysis

² **G**eometry and **T**racking 4 is used for Monte-Carlo simulation

data. Thus a data set similar to real data is produced, which can be used to determine the aforementioned reconstruction efficiency.

3.2.2 Often used physical relations

As the analysis makes use of certain methods and relations quite often, these are presented in this subsection to avoid repetition. All relations can be looked up in for example [17].

Four-vectors

A four vector is made up of four components as the name suggests. These can be time and three space coordinates or energy and three momentum components.

$$\mathbf{p} = \begin{pmatrix} E \\ p_x \\ p_y \\ p_z \end{pmatrix} \text{ or } \mathbf{x} = \begin{pmatrix} t \\ x \\ y \\ z \end{pmatrix} \quad (3.1)$$

Again, as in this whole work, the natural units ($c = 1$) were used. One advantage of momentum four vectors is their square giving the invariant mass.

$$p^\mu p_\mu = E^2 - |\vec{p}|^2 = M^2 \quad (3.2)$$

The term invariant mass originates from its property of being invariant under LORENTZ transformations and thus does not change when boosted into the center of mass frame (cms).

Reconstruction - all decay particles measured

Since all decays and reactions have to fulfil the conservation of energy and momentum, the four vectors have to be conserved to. For example in the reaction $\pi^0 \rightarrow \gamma\gamma$ is:

$$\mathbf{p}_\gamma + \mathbf{p}_\gamma = \mathbf{p}_{\pi^0} \quad (3.3)$$

Therefore the four vectors of two found four vectors can be added and squared to calculate the mass of the π^0 in this example. This makes particle identification possible, even if their mean lifetime is too short to detect the particles themselves.

Reconstruction - one particle not measured

This method originates from the same idea as the equation

$$\mathbf{p}_1 + \mathbf{p}_2 = \mathbf{p}_3 + \mathbf{p}_4 \quad (3.4)$$

can be rearranged and thus particles which cannot be detected (for example a neutral particle in the forward spectrometer) can be reconstructed when knowing the initial state particles. This is called *missing mass*. Furthermore, if not differently stated, the term missing mass will refer to the incoming

photon and the proton at rest as initial state particles in this work. The final state particles will be declared.

3.2.3 Cross section

The cross section is a measure of the probability of a certain reaction [5]. The total cross section σ_{tot} can be calculated as [5]

$$\sigma_{\text{tot}} = \frac{\text{Amount of reactions per time}}{\text{Amount of particles in the beam per time} \times \text{Amount of target particles per area}}. \quad (3.5)$$

This observable has the unit m^2 but is mostly given in [5]

$$1 \text{ barn} = 1 \text{ b} = 10^{-28} \text{ m}^2. \quad (3.6)$$

The cross section might be dependent of the energy and the angle in which the reaction is measured, the differential cross section is often stated [5]:

$$\frac{d\sigma(E, \theta)}{d\Omega}. \quad (3.7)$$

Here the Ω denotes the solid angle

$$\Omega = \int_{\phi_1}^{\phi_2} \int_{\theta_1}^{\theta_2} \sin(\theta) d\theta d\phi. \quad (3.8)$$

Furthermore it shall be explained how the differential cross section will be obtained in this work. To begin with the amount of reaction particles $N(\theta, E_\gamma)$ (in this case the $\Lambda(1520)$) is determined. The different methods of reconstructing the $\Lambda(1520)$ will be listed later. In addition it has to be known how many particles of the reaction are even detected, as no detector has a detection efficiency of 100%. Therefore simulated data is analysed, which allows for knowing the amount of particles that were created and the amount of particles detected. This is explained more thoroughly in section 5.2.3. The result of this is the reconstruction efficiency

$$\varepsilon(\theta, E_\gamma) = \frac{\text{Amount of detected particles}}{\text{Amount of generated particles}}. \quad (3.9)$$

Thirdly the flux of photons $N_\gamma(E_\gamma)$ is needed. This is determined by *GIM* and *FluMo* (see paragraph 3.1.5).

The last two quantities needed are the solid angle Ω and the proton target area density. The first can be calculated as this work only concentrates on forward going K^+ ($\cos(\theta_{\text{CMS}}) > 0.9$)

$$\Omega = \int_0^{2\pi} \int_{\theta_1}^{\theta_2} \sin(\theta) d\theta d\phi = 2\pi \cdot [\cos(\theta)]_{\theta_1}^{\theta_2} = 0.2 \cdot \pi. \quad (3.10)$$

The latter is

$$\rho = 4.237 \times 10^{-8} \frac{1}{\mu\text{b} \cdot \text{cm}}$$

for liquid hydrogen as it is used in this work. To get the area density, ρ has to be multiplied by the length of the target l .

Therefore the cross section can be calculated as

$$\frac{d\sigma(E_\gamma, \theta)}{d\Omega} = \frac{N(\theta, E_\gamma)}{\varepsilon(\theta, E_\gamma) \cdot \rho \cdot l \cdot N_\gamma(E_\gamma) \cdot \Omega}. \quad (3.11)$$

Theoretically the solid angle and beam energy E_γ would have to be infinitesimally small to be the exact cross section, but as it is always limited by the resolution of the detectors, this can never be achieved. However since the cross section will not change significantly over this small solid angle or beam energy, it is sufficient.

Particle selection

Before any analysis can be made, it has to be determined how to select the different particles. The forward K^+ is detected in the forward spectrometer as well as protons and K^- . The particles are selected by their charge and mass. To find the exact mass range with which the particles can be selected, a Voigtian fit is used, which will be explained later on.

The π^0 can be detected in the *BGO Rugby Ball* as it decays into two photons that are measured. Again a Voigtian fit is used to find a mass range with which to select the π^0 in the mass spectrum of two photons combined.

The *BGO Rugby Ball* will also be used to find a photon from the decay of the Σ^0 , but this will be explained in section 5.2.2.

A Voigtian distribution generally means the convolution of a Gaussian distribution and a Breit-Wigner distribution.

$$\text{Gaussian: } f(x) = \frac{e^{-x^2/(2\sigma^2)}}{\sigma\sqrt{2\pi}} \quad (4.1)$$

$$\text{Breit-Wigner: } g(x) = \frac{\Gamma_{\text{BW}}}{\pi(x^2 + \Gamma_{\text{BW}}^2)} \quad (4.2)$$

$$\text{Voigt: } h(x) = (f * g)(x) = \int f(\tau)g(x - \tau)d\tau. \quad (4.3)$$

The Voigtian curve depends on the σ (standard deviation) of the the Gaussian shape and the Γ (Half Width Half Maximum) of the Breit-Wigner shape. As most particles have a smaller natural width than the detector resolution, the peak should be well described by a Gaussian distribution. However, the Voigtian profile has better results and is therefore used. The width of of Voigtian profile can be approximated by ([18], [19])

$$\Gamma_h \approx 0.5343 \cdot 2 \cdot \Gamma_{\text{BW}} + \sqrt{0.2169 \cdot 2 \cdot \Gamma_{\text{BW}}^2 + 8 \cdot \ln 2 \cdot \sigma^2}. \quad (4.4)$$

With these fits a selection in mass can be estimated to select the particles. When choosing the selection mass range one has to find the tightest possible mass range without losing to much of the data. It is not useful to exclude most of the data nor is it effective to include a lot of background.

4.1 Resolution of particles in the forward spectrometer

The forward spectrometer measures the momentum from the curvature of the track and the β -factor¹ from the time of flight. This information can be used to calculate the mass from the relativistic momentum. In the resulting mass spectrum, the K^+ is difficult to see as the scaling is dominated by the proton and pion 4.1(a). Fortunately the amount of π^+ is approximately the same as π^- and further background in the forward spectrometer as can be seen in figure 4.1. Therefore the mass spectrum from negative particles is subtracted from the one of positive particles. This works since the background from pions should be similar in both cases, but there should be no negative particles at the mass of a proton and only few at the K^+ mass as can be seen in figure 4.1(b). The resulting histogram is shown along with a fit in figure 4.2(a). Finally a fit is made to the resulting histograms. The used fit function is the Voigtian profile mentioned above with the background being estimated by a polynomial of third order. This background is not of interest for this work and is only used to improve the Voigtian fit. The results of these fits are presented in table 4.1. Moreover the resulting fits are shown in figure 4.2.

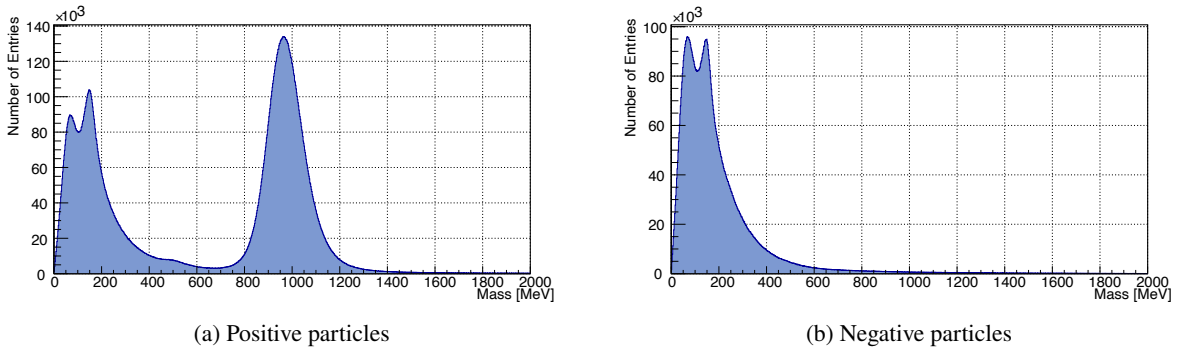


Figure 4.1: Mass of particles in the forward spectrometer with momentum correction for K^+ and K^- respectively.

It has to be investigated, which mass range is optimal for the selection. Therefore different ranges will be examined. In figure 4.3 the determined FWHM as well as the double FWHM are shown in red and blue respectively. For the proton it will be possible to use the double FWHM as there is little background and thus the whole peak can be included. Figure 4.1(a) shows that the kaon peak is overlapping with the pion peak. Therefore the double FWHM would include a lot of background and the FWHM is chosen.

Peak	K^+	p
Mean [MeV]	505.9 ± 0.2	970.9220 ± 0.0002
Width [MeV]	68 ± 2	86.2981 ± 0.0002
σ [MeV]	35 ± 1	64.1945 ± 0.0002
Γ_{BW} [MeV]	42 ± 2	19.0799 ± 0.0002

Table 4.1: Fit parameter for the K^+ shown in figure 4.2(a) and the proton shown in figure 4.2(b).

¹ This term denotes the fraction of the velocity and the speed of light: $\beta = \frac{v}{c}$. With natural units this means $\beta = v$.

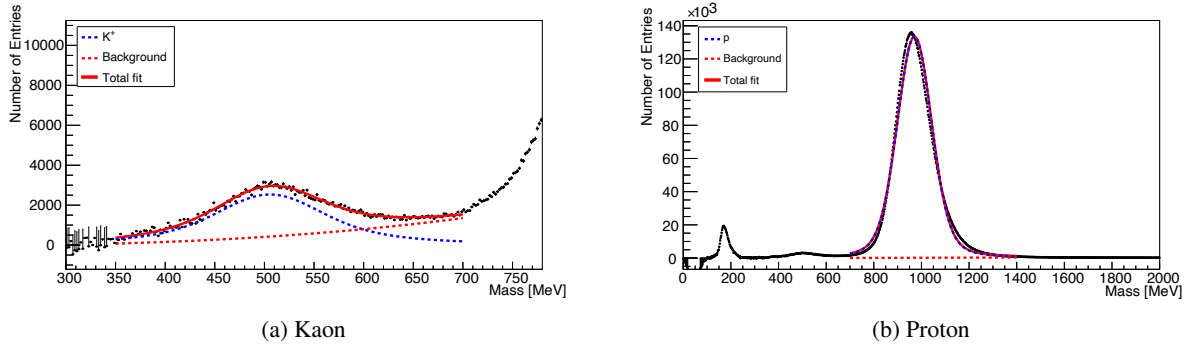


Figure 4.2: Fits to the mass of particles in the forward spectrometer (difference of positive and negative particles).

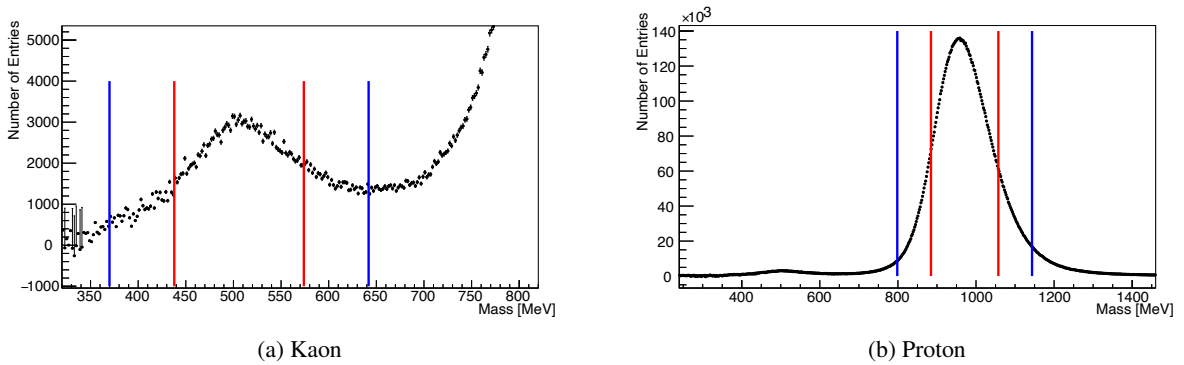


Figure 4.3: Cuts to the mass of particles in the forward spectrometer determined by the fits. The red and blue lines represent the FWHM and twice the FWHM respectively.

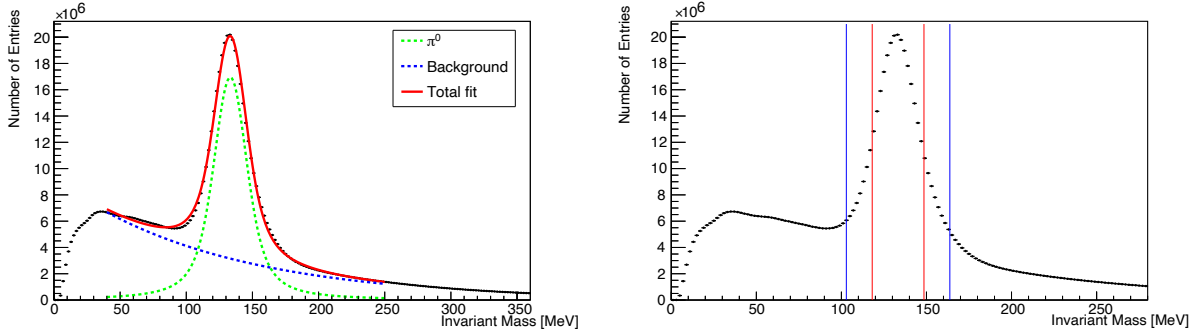
4.2 Resolution of π^0 in the *BGO Rugby Ball*

The width of the invariant mass of the π^0 . Therefore a Voigtian shape is fitted to the invariant mass of two photons in the *BGO Rugby Ball*. To pay attention to the background, an exponential distribution is fitted. This is only done to roughly fulfil the shape and has no physical reason. The fit is shown in figure 4.4(a). Clearly the fit deviates from the data at lower energies than the peak. However as this is just an estimation of the width, these parts do not matter much as long as the peak itself is well described. The result is

$$\begin{aligned}
 m &= (133.323 \pm 0.001) \text{ MeV} \\
 \Gamma &= (15.211 \pm 0.006) \text{ MeV} \\
 \Gamma_{\text{BW}} &= (8.850 \pm 0.006) \text{ MeV} \\
 \sigma &= (8.186 \pm 0.005) \text{ MeV}.
 \end{aligned}$$

Here Γ and m denote the width and peak position respectively. Additionally Γ_{BW} is the Breit-Wigner FWHM and σ is the standard deviation of the Gaussian part. Again the different possible mass ranges for the selection are presented in figure 4.4(b). Like in section 4.1 the double and normal FWHM are depicted. As the background is low compared to the peak, the double FWHM is used to select the π^0 .

These selection criteria make the identification of different particles possible, which can be used in the following analysis.



(a) Invariant mass of two photons in the *BGO Rugby Ball*. (b) Different selection ranges for the mass of the π^0 . In blue the range with $2 \cdot \Gamma$ and in red the one with Γ is shown.

Figure 4.4: Invariant mass of two photons detected in the *BGO Rugby Ball* with fits and resulting mass ranges for selection.

Determination of the differential cross section of the reaction $\gamma p \rightarrow K^+ \Lambda(1520)$

The aim in this chapter is to determine the differential cross section for the reaction $\gamma p \rightarrow K^+ \Lambda(1520)$. First a selection of the reaction has to be made. Afterwards the amount of events at a certain beam energy can be used to calculate the differential cross section. As different methods and decay channels are examined, this chapter is divided into two parts. In the first two exclusive analyses of decay channels including charged particles are presented. This alternative methods are not preferred, but are included as other experiments utilised these channels and it can still be improved in the future.

Afterwards the successful analysis is shown. It includes two inclusive methods, where only particles are required which are part of every decay chain, and an exclusive method that focused on the neutral decay of the $\Lambda(1520)$ into $\Sigma^0 \pi^0$. As the *BGO Rugby Ball* is excellent at detecting photons over a large angular range, this channel can be more easily identified than the channels with only charged particles.

5.1 Identification of decays with charged particles

The decay of the $\Lambda(1520)$ into only charged particles is difficult as a wide angular range of the experiment is optimised to detect neutral particles. Still identification of charged particles is possible.

5.1.1 $K^+ \Lambda(1520) \rightarrow K^+ p K^-$

This channel was used to analyse the $\Lambda(1520)$ in the photoproduction analysis of BARBER ET AL. [20]. To identify p and K^- in the central detector is difficult, therefore the particles are searched for in the forward spectrometer.

This will be difficult, because the $\Lambda(1520)$ is produced with little momentum if the K^+ is detected at forward angles. As a solution only one of the decay particles of the $\Lambda(1520)$ will be required in the forward spectrometer and the missing momentum will be examined. Not only the missing mass will be calculated but also the angle difference between charged particles detected in the *BGO Rugby Ball* and missing momentum.

The first method to identify this reaction is to calculate the missing mass to K^+ and K^- , both detected in the forward spectrometer, theoretically giving the mass of a proton. The result is shown in figure 5.1. Only few events are observed and no peak can be seen. This is a result of the difficulty of detecting

two charged particles in the forward spectrometer and therefore at small angles. There is also a lot of background from pions inside the mass range for selection. Hence this method is not useful to identify the correct reaction as statistics are very poor and additionally dominated by background.

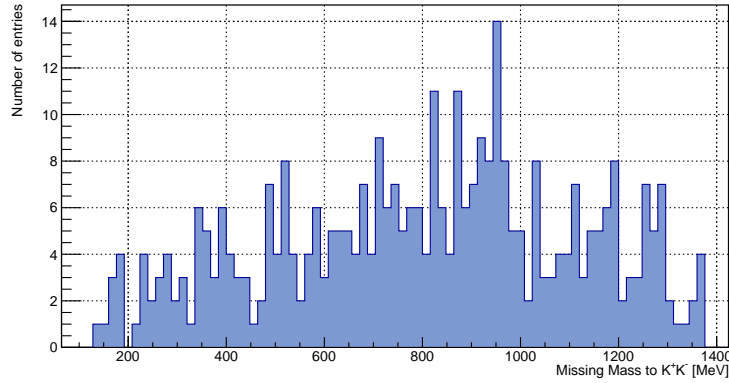


Figure 5.1: Missing mass to K^+ and K^- , both detected in the forward spectrometer.

The logical next step is to look at the missing mass to K^+ and p , which should be the mass of a kaon. As before the K^+ and protons are only registered in the forward spectrometer. The resulting histogram is depicted in figure 5.2. This time a broad peak at about 450 MeV is seen but a clear identification is difficult. Additionally the background is dominant again.

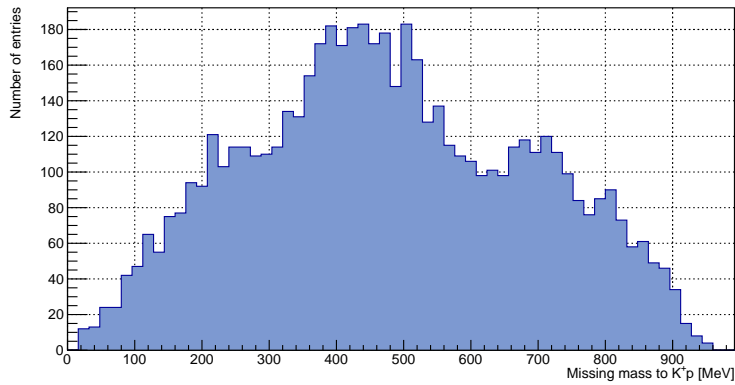


Figure 5.2: Missing mass to K^+ and p in the forward spectrometer.

The structure at 450 MeV could still be K^- . This can be examined by calculating the total angle difference between these reconstructed K^- and charged events in the *BGO Rugby Ball* which could be K^- . If a peak at an angle difference of 0° and a reconstructed K^- mass of about 500 MeV can be seen, these could be the K^- . However, as is shown in figure 5.3, only a peak at 60° can be seen, so it is not possible to identify the K^- and therefore also not the reaction channel. Altogether this channel could not be identified with the applied methods. Thus a different method will be tried for the second channel including charged particles.

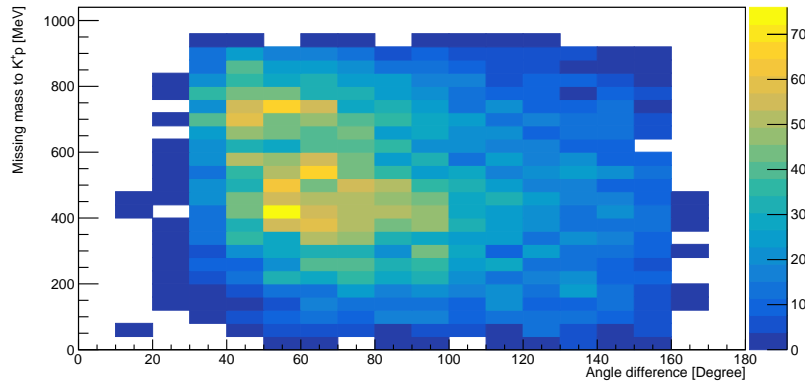


Figure 5.3: The missing mass to proton and K^+ plotted against angle difference of charged particles in the *BGO Rugby Ball* and reconstructed K^- .

5.1.2 $K^+ \Lambda(1520) \rightarrow K^+ \Sigma^+ \pi^-$

This channel was used by *CLAS* for their analysis [21]. The Σ^+ decays into a proton and a π^0 or a neutron and a π^+ [1]. Since both the neutron and the π^+ are hard to detect it is not effective to focus on that decay. Instead the invariant mass of the $p\pi^0$ system is used to reconstruct the Σ^+ . The proton is identified in the forward spectrometer and the π^0 in the central detector.

The result of this is shown in figure 5.4. In the histogram a peak a little below 1 200 MeV is observed, which is the range in which one would expect the Σ^+ to be. However the peak is on top of a very large background. This background makes a clean identification of the Σ^+ difficult. Additionally a π^- has to be identified in the central detector to reconstruct the $\Lambda(1520)$. Altogether this means that the identification of this reaction channel might be possible but includes so much background that no further analysis can be made. Thus an inclusive analysis as well as an identification of the decay into neutral particles follows.

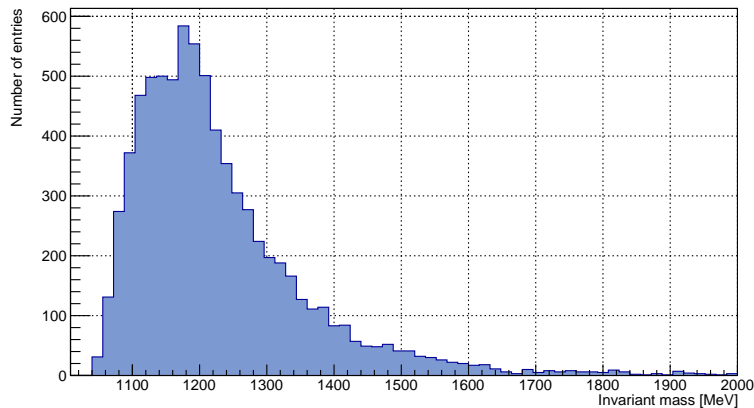


Figure 5.4: Invariant mass of p detected in the forward spectrometer and π^0 detected in the *BGO Rugby Ball*.

5.2 Inclusive identification of $K^+ \Lambda(1520)$

In the following section, data from November 2018 is used. This data has been taken with an 11 cm long liquid hydrogen target. In total about $1.9 \cdot 10^9$ events were registered in 18 days.

5.2.1 Requirements for the identification of $K^+ \Lambda(1520)$

So far it is clear that searching for the charged channels exclusively is not easily possible. Therefore this work will use the following three ways of identifying the reaction $\gamma p \rightarrow K^+ \Lambda(1520)$.

Firstly only a K^+ is identified in the forward spectrometer at an angle of $\cos(\theta_{K^+, \text{CMS}}) > 0.9$. This means, that the K^+ detected in the forward spectrometer will be boosted into the centre of mass frame and the polar angle is determined. Afterwards the missing mass to the K^+ is calculated. This method includes all decay channels of $\Lambda(1520)$.

Secondly an additional π^0 reconstructed from photons in the *BGO Rugby Ball* is required. Since most decay channels include a π^0 at some point, almost all decay channels contribute here. This will be further discussed in section 5.2.2.

Thirdly a method will be used that focuses on the decay $\Lambda(1520) \rightarrow \pi^0 \Sigma^0$. The Σ^0 decays into a Λ and a photon. The photon always has the same energy in the rest frame of the Σ^0 as will be shown later. Thus in addition to the K^+ and the π^0 a photon with this energy will be required. Later on, this photon with the right energy in the rest frame of the Σ^0 will only be called single photon.

Finally simulated line shapes are fitted to the missing mass to K^+ in all three methods. The result is the yield of $\Lambda(1520)$ from which the cross sections can be determined.

Before the differential cross section is determined, some properties of the different methods are explained for a more profound understanding.

5.2.2 Properties of the different requirements

Depending on the requirement made for the selection of the reaction the results have some particularities that shall be explained in this section.

Only K^+ required

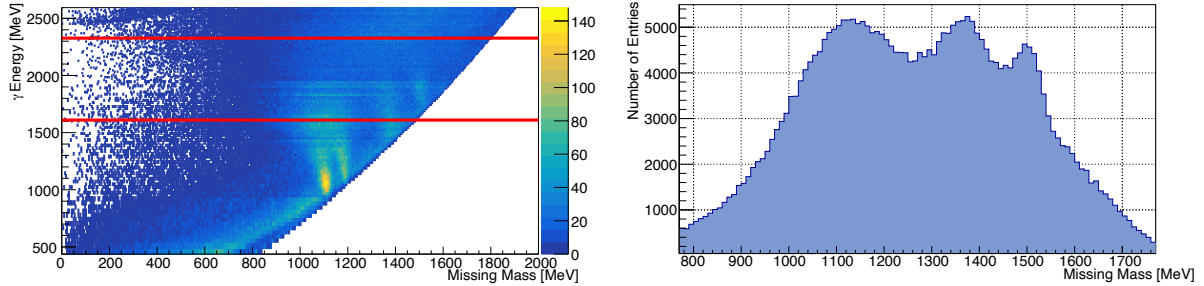
The first requirement is that of a K^+ being detected in the forward spectrometer at a centre of mass angle of $\cos(\theta_{K^+, \text{CMS}}) > 0.9$. Figure 5.5(a) shows the missing mass to a K^+ at angles of $\cos(\theta_{K^+, \text{CMS}}) > 0.9$ against the corresponding beam energy. The horizontal lines can be explained by the changing geometry of the tagger hodoscope, which results in a different energy resolution at different energies.

Figure 5.5(b) shows the missing mass to a K^+ at beam energies $E_\gamma = (1\,610 - 2\,327)$ MeV. This energy range is chosen since photoproduction of $\Lambda(1520)$ is only possible at $E_\gamma > 1\,690$ MeV. This can be calculated by using masses from [1]:

$$\begin{aligned} (E_\gamma + m_p)^2 - E_\gamma^2 &\geq (m_{K^+} + m_{\Lambda(1520)})^2 \\ \Leftrightarrow E_\gamma &\geq \frac{1}{2m_p} \left((m_{K^+} + m_{\Lambda(1520)})^2 - m_p^2 \right) \\ \Rightarrow E_\gamma &\geq (1\,686 \pm 1) \text{ MeV.} \end{aligned}$$

Since all particles have a width, a energy lower than that value is used in order not to exclude relevant events. The upper limit is chosen, since no signal was visible at higher energies.

Three peaks are visible. The first is broad, has a mean value of about 1 100 MeV and can therefore be assigned to the Λ and the Σ^0 . The next peak has its highest point at about 1 400 MeV and can therefore be interpreted as the $\Lambda(1405)$ and the $\Sigma(1385)$. Lastly the third peak is around 1 500 MeV and is consistent with the $\Lambda(1520)$. Thus it is possible to see the $\Lambda(1520)$ without further requirements.



(a) Missing mass against beam energy. The projected range on the right is shown with the red lines.

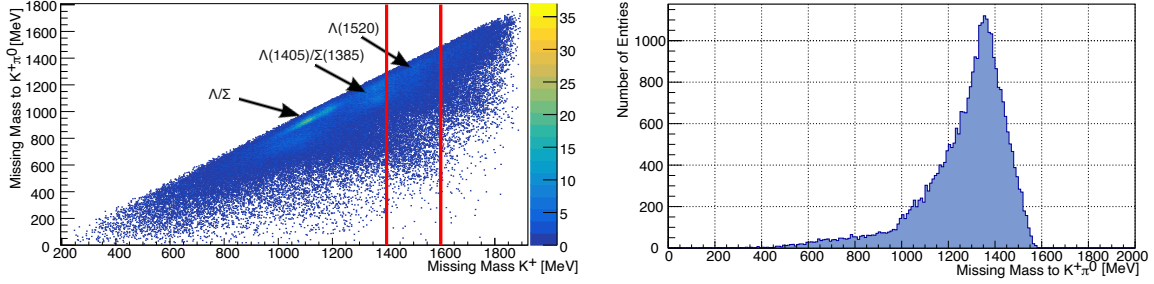
(b) Projection of 5.5(a) at energies (1 610-2 327) MeV.

Figure 5.5: Missing mass to K^+ at $\cos(\theta_{K^+, \text{CMS}}) > 0.9$.

K^+ and π^0 required

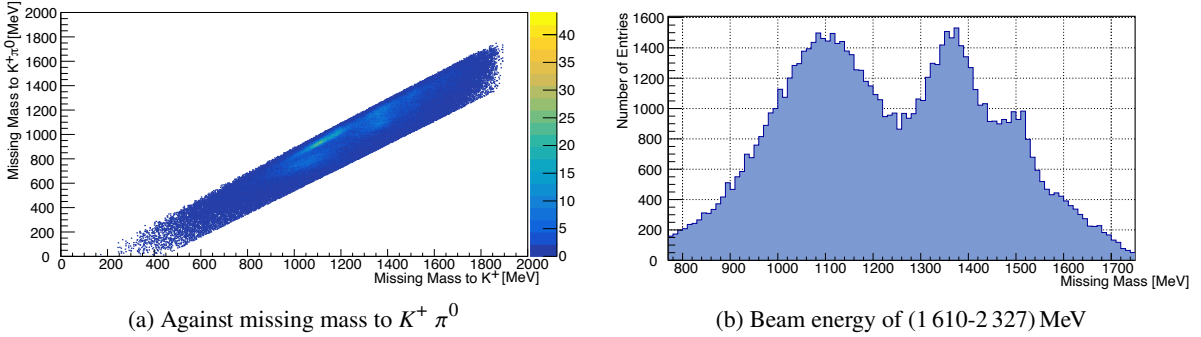
Even though the $\Lambda(1520)$ is already seen without further requirements, the background can be reduced by requiring an additional π^0 . Figure 5.6(a) shows the missing mass to $K^+ \pi^0$ against the missing mass to K^+ for real data. As can be seen, the signal is close to the sharp edge while a lot of background is below that. This is emphasised by the projection of the histogram 5.6(b). With the additional help of simulated data a two dimensional cut was heuristically determined. All events that have a missing mass to $K^+ \pi^0$ that is more than 415 MeV below the missing mass to K^+ are sorted out to reduce background. The result is depicted in figure 5.7(a).

Just like in section 5.2.2 the missing mass to K^+ is shown for an energy range of (1 610-2 327) MeV, but this time after an additional π^0 is required and the two dimensional cut is made, in figure 5.7(b). The background is reduced while the shapes of the peaks are clearer.



(a) Missing mass to K^+ and π^0 versus the missing mass to K^+ . The projected range on the right is shown with the red lines. (b) Projection of missing mass to K^+ (1 400-1 600) MeV of the histogram on the left.

Figure 5.6: Missing mass to K^+ after requiring an additional π^0 . Full possible range of E_γ .



(a) Against missing mass to $K^+ \pi^0$

(b) Beam energy of (1 610-2 327) MeV

Figure 5.7: Missing mass to K^+ after two dimensional cut and additional π^0 .

Double Peak in the Missing Mass

In figure 5.8 the plot of missing mass to $K^+ \pi^0$ against missing mass to K^+ is shown again, but this time for simulated data to emphasise the signal. While the result for the $\Lambda(1405)$ is a single peak at a missing mass to K^+ of about 1 400 MeV and missing mass to $K^+ \pi^0$ of about 1 200 MeV and therefore the reaction $K^+ \Lambda(1405) \rightarrow K^+ \Sigma^0 \pi^0$, the plot for the $\Lambda(1520)$ shows two peaks, one of which is the analogue to the peak of the $\Lambda(1405)$. The explanation for the other peak are the additional decay channels of the $\Lambda(1520)$, namely into $p K^-$ and $\pi \pi \Lambda$, which are not present in the decay of the $\Lambda(1405)$. These channels also include π^0 . Contrary to the $\Lambda(1405)$ those are not correlated to a Σ^0 and therefore a broad, smeared out peak just a π^0 -mass below the missing mass to a K^+ appears as figure 5.9 shows. In this figure the $\Lambda(1670)$ was simulated too.

This double peak is an indication that the reaction is well understood and that an inclusive analysis is made when requiring the π^0 . In order to perform an exclusive analysis further requirements have to be made.

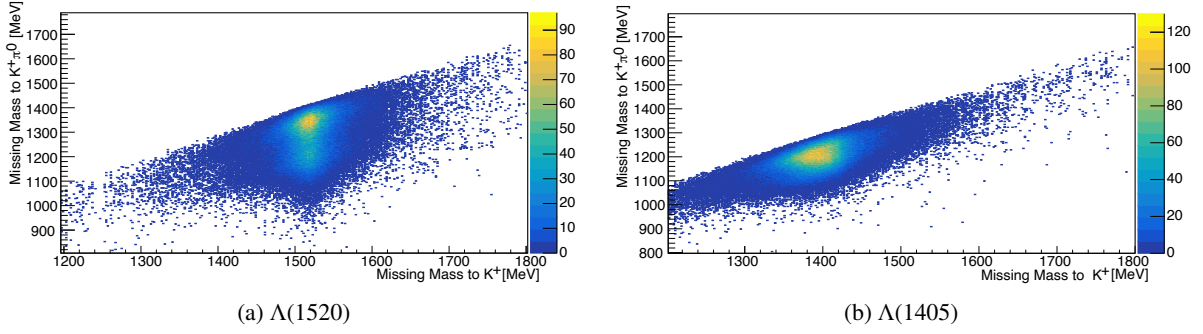


Figure 5.8: Missing mass to K^+ and π^0 versus the missing mass to K^+ in case of simulated $\Lambda(1520)$ and $\Lambda(1405)$. Data was simulated for 100 million events each time.

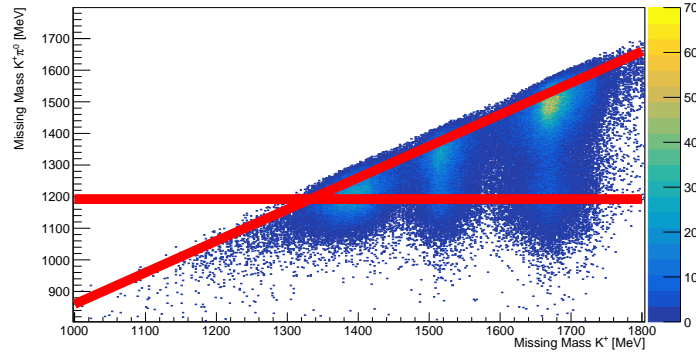


Figure 5.9: Simulated data of the $\Lambda(1405)$, $\Lambda(1520)$ and $\Lambda(1670)$. Each time, 10 Million events were simulated. Missing mass to K^+ and π^0 plotted against the missing mass to K^+ . The horizontal line marks the mass of the Σ^0 and the diagonal line depicts the missing mass to K^+ minus the mass of a π^0 and thus a line, where the peak from other channels than $\Sigma^0 \pi^0$ will approximately be.

K^+ and π^0 with additional photon required

The last selection requires an additional photon with the correct energy in the rest frame of the Σ^0 . This energy can be calculated as (masses from the PDG [1])

$$\Sigma^0 \rightarrow \gamma \Lambda \quad (5.1)$$

$$\begin{pmatrix} m_{\Sigma^0} \\ 0 \end{pmatrix} = \begin{pmatrix} E_\gamma = |\vec{p}| \\ \vec{p} \end{pmatrix} + \begin{pmatrix} \sqrt{m_\Lambda^2 + |\vec{p}|^2} \\ -\vec{p} \end{pmatrix} \quad (5.2)$$

$$\Leftrightarrow 2m_{\Sigma^0} E_\gamma = m_{\Sigma^0}^2 - m_\Lambda^2 \quad (5.3)$$

$$\Rightarrow E_\gamma = \frac{m_{\Sigma^0}^2 - m_\Lambda^2}{2m_{\Sigma^0}} = (74.476 \pm 0.023) \text{ MeV}. \quad (5.4)$$

The Σ^0 is reconstructed from the missing momentum to the K^+ and π^0 . The single photon additionally has to fulfil the condition that combined with the photons used to reconstruct the π^0 it has to have a mass

smaller or bigger than a pion¹. Thus it is clear that the single photon does not belong to the decay of a π^0 . The energy of the single photons in the rest frame of the Σ^0 is shown in figure 5.10. A peak around 70 MeV can be seen, which is consistent with the energy of the Σ^0 decay photon. For further analysis only events are selected where the energy of the single photon is between (50-100) MeV, which is shown with the red lines in the figure. Otherwise all the steps are identical to the sections 5.2.2 and 5.2.2. The

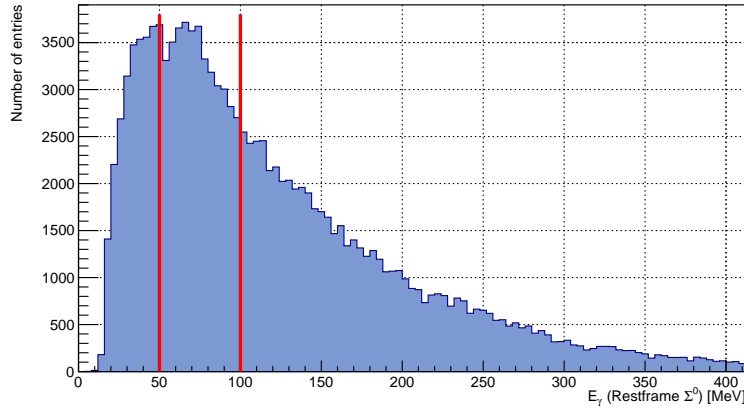
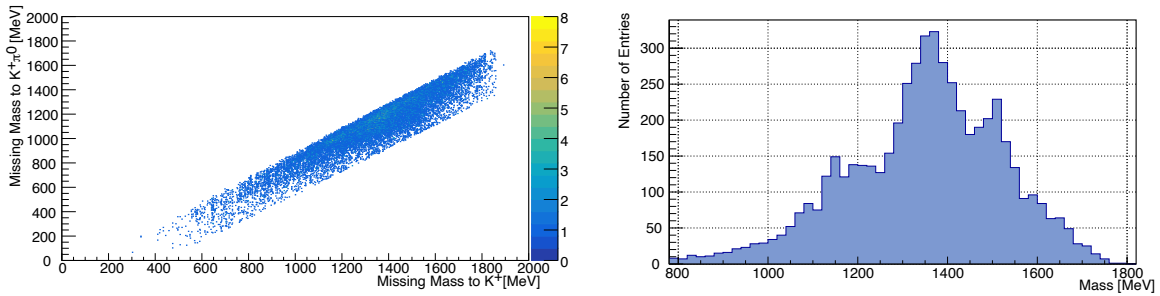


Figure 5.10: Energy of the single photon in the *BGO Rugby Ball* boosted into the restframe of the reconstructed Σ^0 . The red lines represent the selection of the single photon.

result is shown in figure 5.11. The peak of the Λ and Σ^0 is visibly smaller as they do not decay into $\Sigma^0 \pi^0$. Thus the peak from $\Lambda(1520)$, $\Sigma(1385)$ and $\Lambda(1405)$ are more visible. The overall number of events is strongly reduced resulting in an increase of statistical uncertainty.

This error has an influence on the fits of the line shapes to the data, which will be performed after estimating the reconstruction efficiency.



(a) Missing mass to $K^+ \pi^0$ against missing mass to K^+ . Full beam energy range. (b) Missing mass to a K^+ for beam energies of (1610-2327) MeV

Figure 5.11: Missing mass to K^+ after two dimensional cut and requirement of π^0 with additional photon.

¹ This means that the invariant mass of the sum of the four vectors is outside of the cut determined for the π^0 in section 4.2.

5.2.3 Reconstruction Efficiency

In order to determine the cross section it is necessary to have knowledge about the reconstruction efficiency, which describes the fraction of detected particles. The value is affected by detector properties (for example detector efficiency), physical setup (particles could move in directions where no detector is placed) and the particle selection. Since the detector is the only device to detect the particles it is not possible to know all existing particles in real data. Therefore simulated data is analysed, because the number of generated particles is known in that case. The analysis is exactly the same as with real data and in every different cut from section 5.2.1 the found particles are registered. Additionally all the generated kaons with $\cos(\theta_{K^+, \text{CMS}}) > 0.9$ are saved. The fraction of the two then gives the reconstruction efficiency. The resulting histogram is shown in figure 5.12.

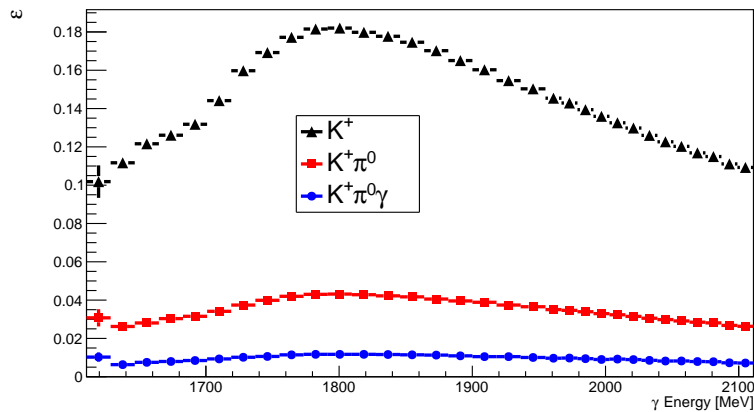


Figure 5.12: The reconstruction efficiencies for the different requirements. Black triangles show the requirement of just a K^+ , red squares represent a K^+ with π^0 and the blue circles a K^+ with π^0 and γ .

5.2.4 Determination of the cross section of $\gamma p \rightarrow K^+ \Lambda(1520)$

The cross section is an important measure of a reaction and will be calculated as explained in section 3.2.3. The reconstruction efficiency has been determined in section 5.2.3 and the proton target density is given in section 3.2.3. Furthermore the amount of detected $\Lambda(1520)$ will be extracted out of the histograms presented in the sections above while the measured flux is shown in figure 5.13. The visible step at about 1950 MeV is a result of the changing geometry of the tagger detector.

The fits are performed in the following way: As a first step, all potentially relevant channels are simulated. These simulations are used to get the line shapes of the different channels in the missing mass to a K^+ . Afterwards the line shapes² are fitted to the real data using a binned likelihood fit from RooFit [22]. As simulated data and real data could have slight shifts due to calibrations, it is allowed to move the line shapes along the horizontal axis. Important however is, that the line shapes are not changed by the fit but only scaled. It is mentioned at this point, that several channels are simulated and fitted, but as some line shapes look very similar, sometimes some channels do not appear in the fit. This however does not affect

² In this context the term line shape denotes the distribution in the missing mass to a K^+ obtained in simulation.

the results as long as the background and the peak of the $\Lambda(1520)$ are well described.

Not all background is simulated reaction channels since π^+ wrongly identified as K^+ also contribute. This part of the background is described by doing the same analysis with a K^- in the forward spectrometer. Only few correctly identified K^- should be detected in the forward spectrometer as the reaction has a positive charge in the initial state. Therefore it can be assumed that the selected K^- are wrongly selected π^- and thus this result can be used as additional background. The fit to the data with requirement of the additional π^0 includes the background channel obtained by analysing the K^- . Nonetheless as statistics did not allow to use the background determined by the analysis requiring the π^0 , the background from the analysis requiring only the K^+ was used. As both methods include all decay channels this should not have an influence on the result. Since exclusive analysis with requirement of the single photon does not include all channels, this background can not be used there.

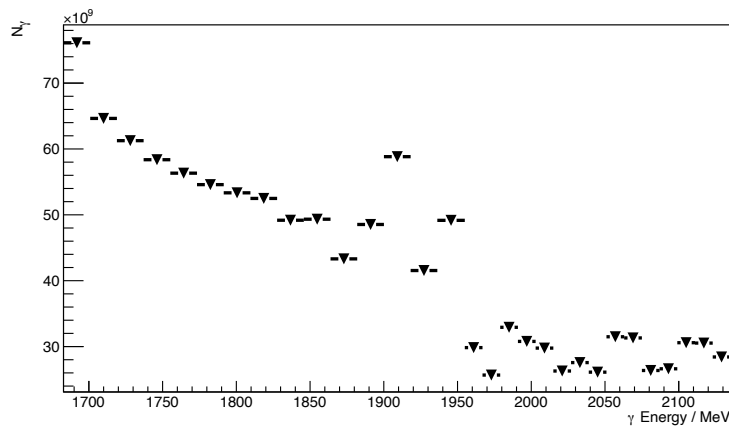


Figure 5.13: Photon flux.

As an example, figure 5.14 shows the fit to the missing mass to a K^+ obtained by requiring just a K^+ at $\cos(\theta_{K^+, \text{CMS}}) > 0.9$ at a beam energy of (1 773-1 828) MeV. For comparison, the fits at the same beam energy with the other requirements are shown in figure 5.15. All other fits can be found in appendix A.1. The range of (1 100-1 700) MeV of the missing mass to a K^+ is used for the fit. Thus the important peaks are included and the background is well described. In a few fits this range is slightly adapted as RooFit has difficulties as soon as single data points are exactly zero or statistical fluctuation get too big. This however does not affect the fits as long as all peaks are still within the range.

As aforementioned the similarities between the line shapes of $\Lambda(1405)$ and $\Sigma(1385)$ causes RooFit to exchange both. In most cases the expected result of two peaks that are on top of each other and result in a broader peak is obtained. Nonetheless sometimes only one line shape is fitted to the data. As long as the background is well described this does not affect the resulting differential cross section. The same applies to the line shapes of Λ and Σ^0 . Therefore the fitted line shapes apart from $\Lambda(1520)$ should be understood as tools to describe the background and the important part of the fits is the peak consistent with the mass of the $\Lambda(1520)$.

The fit is used to determine the yield of the $\Lambda(1520)$ and ultimately the differential cross section can be calculated using formula 3.11, the reconstruction efficiency from section 5.2.3, the photon flux from figure 5.13 and the proton target density. The result is presented in figure 5.16. In general a good agreement between the different requirements is achieved. At energies above 1 900 MeV the cross section

starts to differ from the data published by KOHRI ET AL. [4] as well as from each other. This could be caused by an increased background at higher beam energies, which can lead to imprecise fits. However, this has to be examined further, for example by analysing more data.

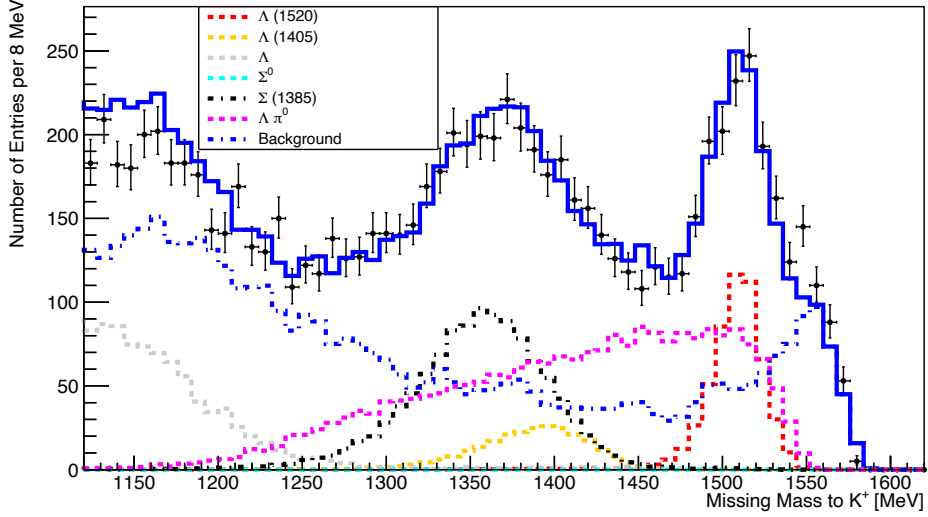


Figure 5.14: Fit to the data with requiring just a K^+ at $\cos(\theta_{K^+, \text{CMS}}) > 0.9$ at beam energies (1 773-1 828) MeV.

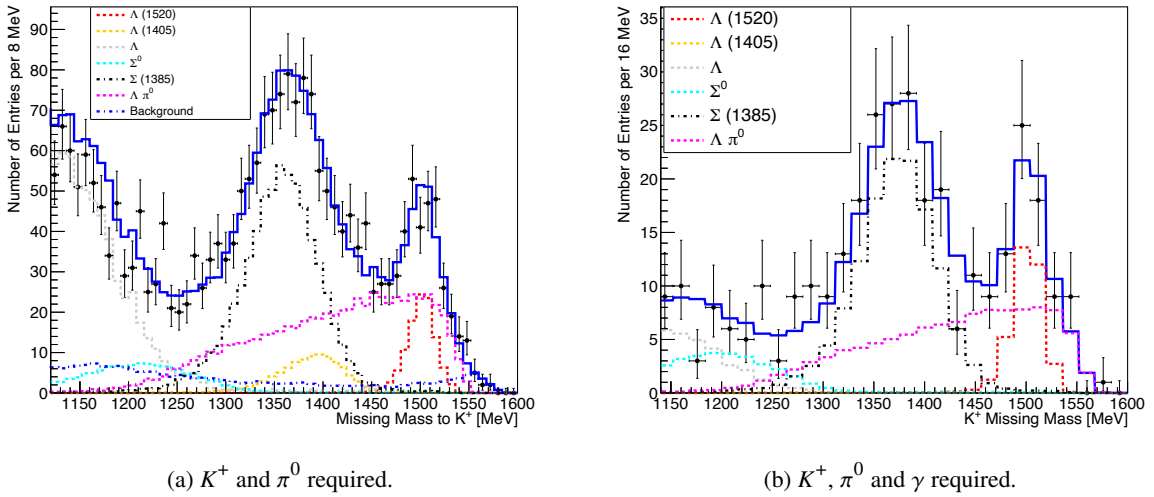


Figure 5.15: Fit to the data with the other requirements at beam energies (1 773-1 828) MeV.

Subsequently the aim will be to split the angle $0.9 < \cos(\theta_{K^+, \text{CMS}}) < 1$ into smaller bins to examine the K^+ going completely forward and therefore a minimal momentum transfer to the $\Lambda(1520)$. This was not possible given the time limit. Nonetheless a calculation of the differential cross sections for three smaller bins in $\cos(\theta_{K^+, \text{CMS}})$ is presented. The results are shown in figure 5.17. As the signal yield is

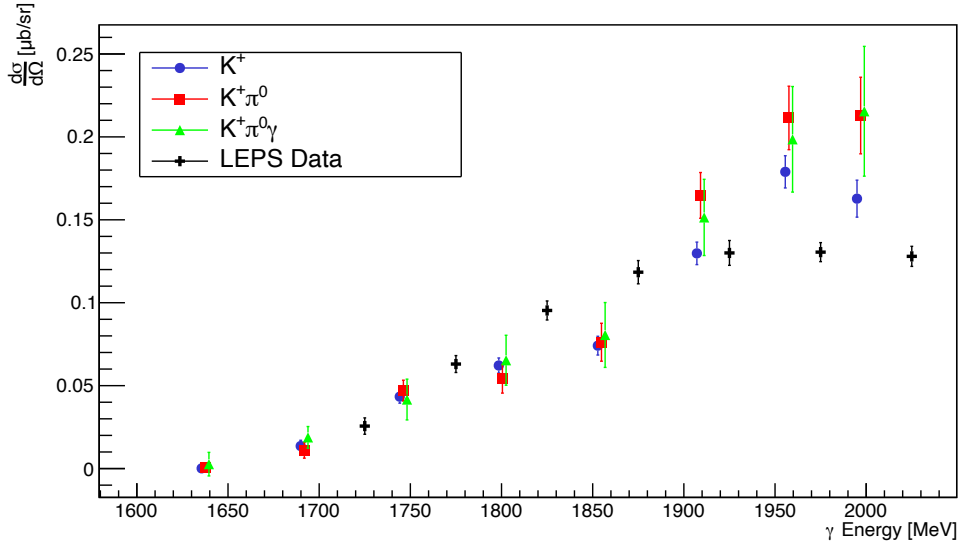


Figure 5.16: Differential cross section determined with the different requirements (as described in the legend). The data points are shifted by 2 MeV for better visibility. The black crosses are results from LEPS [4].

split in three, only a K^+ is required, as this provides the best statistics.

Within the available accuracy no further structures can be observed.

The consistency is checked by averaging the three smaller angle bins and comparing the result with the differential cross section with the requirement of just a K^+ at an angle $0.9 < \cos(\theta_{K^+, \text{CMS}}) < 1$ as shown in figure 5.16. No significant deviations can be observed and the results are consistent with each other as is shown in figure 5.17(b).

Lastly the systematic errors need to be determined.

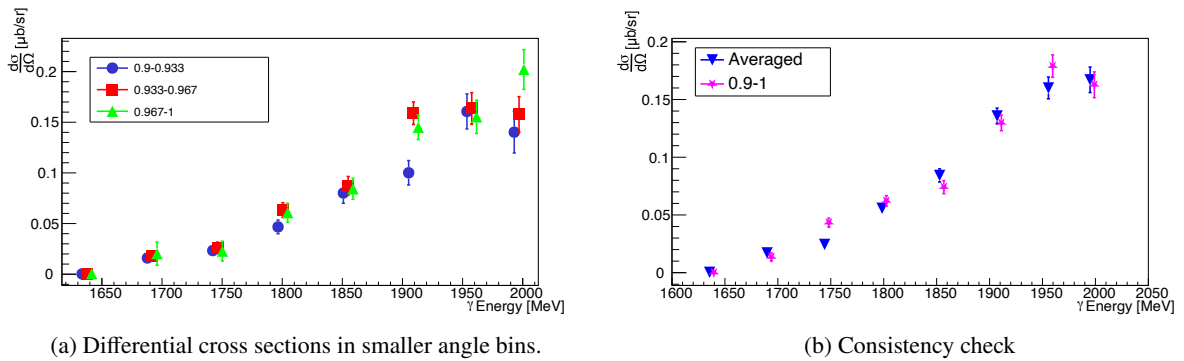


Figure 5.17: Differential cross sections for smaller angle bins. Only a K^+ is required. The numbers in the legend refer to the $\cos(\theta_{K^+, \text{CMS}})$. As a check of consistency the three small bins are averaged and compared to the result in figure 5.16 when requiring only a K^+ . The data points are slightly shifted for better visibility.

5.2.5 Estimation of the systematic errors

To get a measure for the accuracy of the results the systematic errors are estimated. Many universal uncertainties were already estimated in [23] and are shown in table 5.1 together with the systematic errors estimated in this section. Some of the errors might differ as another data set is used in this thesis, but since it can be assumed that the deviation is small, it is a good estimation. The systematic error for the target length was scaled with the fraction of the target lengths since for [23] a shorter target was used than in this thesis and the absolute error remains the same. Additionally the systematic error for the selection of the K^+ has to be estimated as well as the error due to selection and fitting of π^0 and γ .

The relative error is obtained in the following way: Firstly the differential cross section is determined with modified selection or requirements. Then the difference to the cross section as determined in section 5.2.4 with only requiring a K^+ is calculated. This difference is then divided by this cross section.

The error from the selection of the K^+ is estimated by changing the mass range for selection of the K^+ by $\pm 25\%$. A combined error for fitting and selection of π^0 and γ is estimated by comparing the differential cross sections determined with the different requirements in section 5.2.4.

The result is shown in figure 5.18. The weighted mean of the comparison with K^+ and π^0 needed is $\sigma_{\text{sys}} \approx 14.1\%$. For the K^+ , π^0 and γ required it is $\sigma_{\text{sys}} \approx 13.6\%$. Hence an upper limit of a systematic error due to fitting and selection of further particles can be estimated to be $\sigma_{\text{sys, fit}} \approx 14.1\%$. This error is mainly a result of the fitting, as the deviation is smaller when having more selection criteria.

The systematic error due to the selection of K^+ is shown in figure 5.19. The weighted mean is $\sigma_{\text{sys}} \approx 1.4\%$ for the smaller and $\sigma_{\text{sys}} \approx 3.0\%$ for the bigger mass range. Thus a upper limit of about $\sigma_{\text{sys, selection}} \approx 3\%$ can be estimated.

Everything summed up quadratically gives a systematic error of $\sigma_{\text{sys, all}} \approx 16.3\%$.

Source	% Error
Beam spot alignment	4.0
Photon flux	4.0
<i>SciFi2</i> efficiency	3.0
Target wall contribution	2.0
Track time selection	2.0
Target length	0.9
<i>ToF</i> wall efficiency	1.5
<i>MOMO</i> efficiency	1.0
Drift chamber efficiency	1.0
Beam energy calibration	1.0
Modeling of hardware triggers	1.0
Forward track geometric selection	1.0
Fitting and selection of π^0 and γ	14.1
Mass range for the selection of K^+	3.0
Summed quadratically	16.3

Table 5.1: Systematic errors in this analysis. The values apart from the last two are taken from [23].

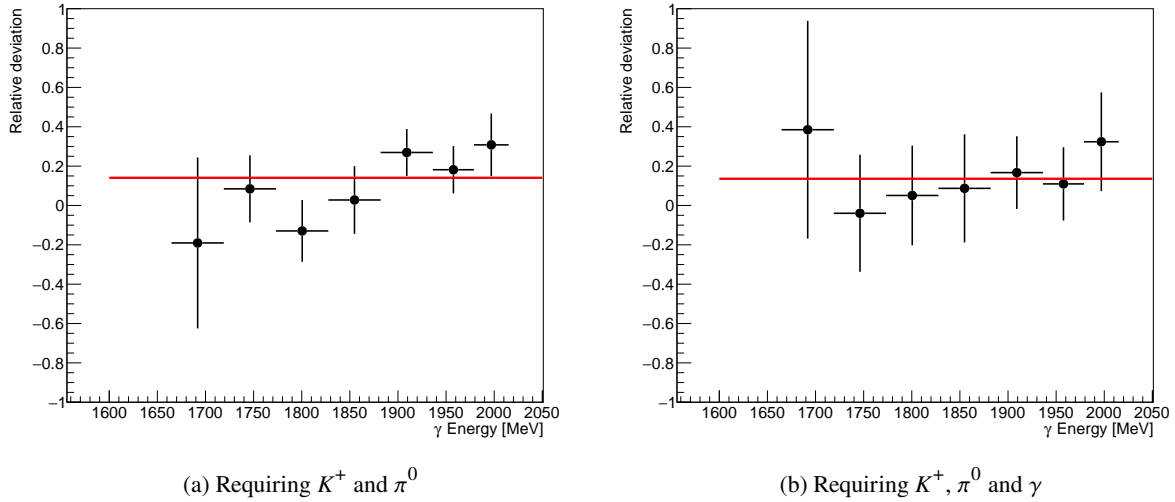


Figure 5.18: Estimation of the systematic error from selection of π^0 (and γ) and the fitting. The red line is the error weighted mean.

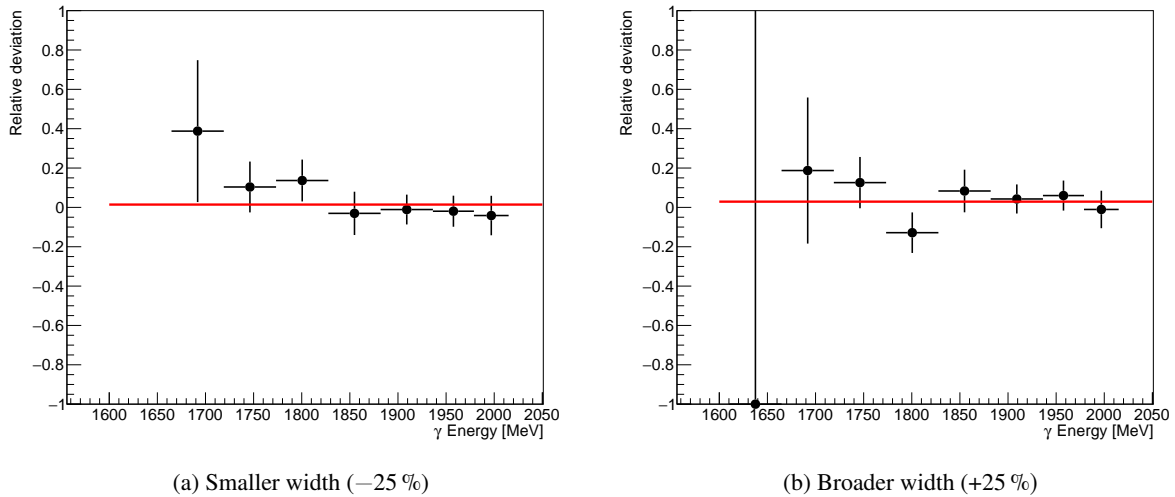


Figure 5.19: Estimation of the systematic error from selection of K^+ . The red line is the error weighted mean.

Summary and outlook

The aim of this thesis was to examine whether a reconstruction of the $\Lambda(1520)$ was possible with the *BGOOD*-experiment at the *ELSA*-facility in Bonn. Different decay channels were investigated. It was not possible to extract the charged decay channels from the $\Lambda(1520)$ but in the decay into $\pi^0\Sigma^0$ the $\Lambda(1520)$ could be identified. The differential cross section for the reaction $\gamma p \rightarrow K^+\Lambda(1520)$ at forward angles of the K^+ ($\cos(\theta_{K^+, \text{CMS}}) > 0.9$) was determined. This was in good agreement with the cross sections determined by *LEPS* [4] with small deviations at a beam energies above 1 900 MeV. More data is available and can be analysed to resolve this deviation in the future.

In this work three channels of the tagger hodoscope were combined. Making use of a second data set the improved statistical accuracy would allow to improve the energy resolution by investigating the reaction in single tagger channels.

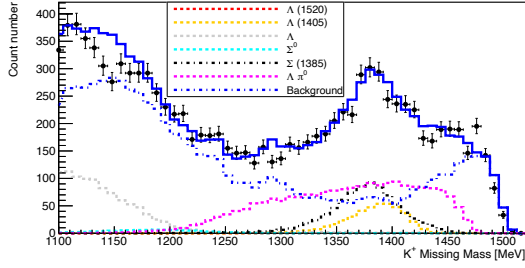
As *LEPS* showed interesting behaviour at energies above 2 000 MeV beam energy, further studies could examine whether different methods were able to analyse higher energies at *BGOOD*. This could include a Cherenkov detector, that is already planned for the experiment, to separate K^+ and π^+ which is an improvement at higher energies. Additional momentum corrections can also improve the resolution in the missing mass to a K^+ .

Summarising it can be concluded that an analysis of the $\Lambda(1520)$ is possible with the *BGOOD*-setup. A further outlook could be a finer resolution in the $\cos(\theta_{K^+, \text{CMS}})$ which can be used to extrapolate the differential cross section to $\cos(\theta_{K^+, \text{CMS}}) = 1$. This value corresponds to a minimal momentum transfer which is needed for a molecular structure like the $\Lambda(1405)$ has.

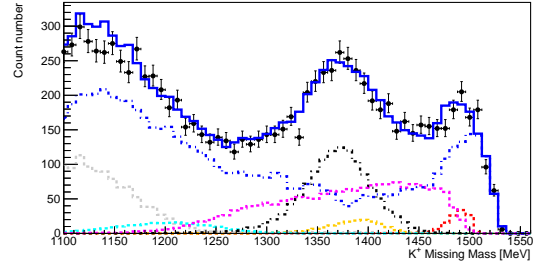
Appendix

A.1 Fits to the missing mass

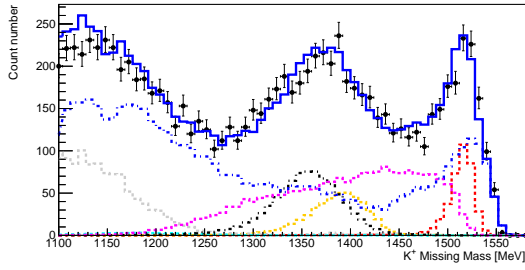
The fits mentioned in section 5.2.4 are depicted here.



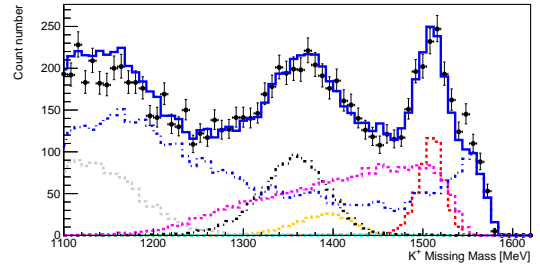
(a) Energy (1 610-1 665) MeV



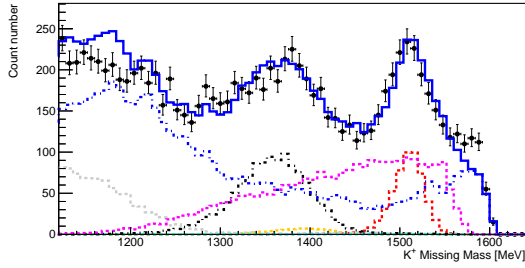
(b) Energy (1 665-1 719) MeV



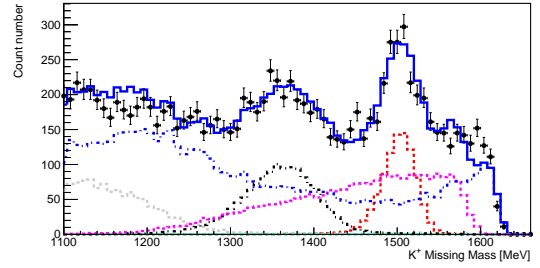
(c) Energy (1 719-1 773) MeV



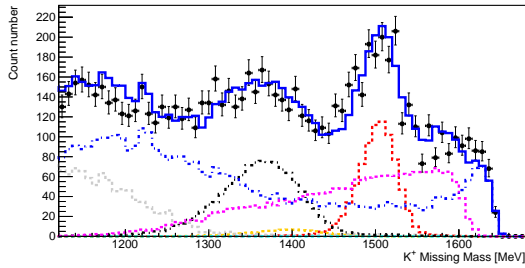
(d) Energy (1 773-1 828) MeV



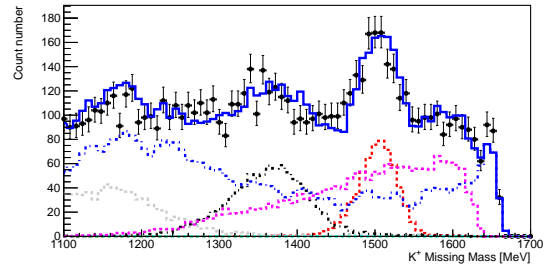
(e) Energy (1 828-1 882) MeV



(f) Energy (1 882-1 936) MeV



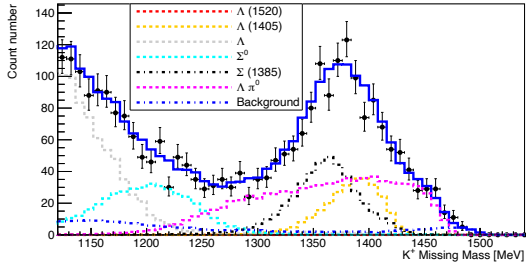
(g) Energy (1 936-1 979) MeV



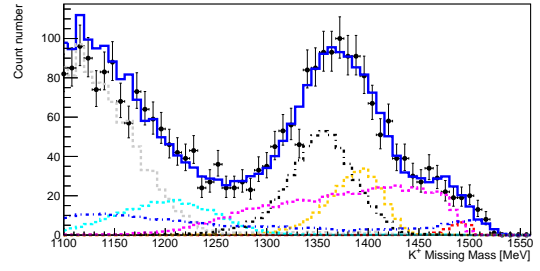
(h) Energy (1 979-2 015) MeV

Figure A.1: Fits to the missing mass to a K^+ at $\cos(\theta_{\text{CMS}}) > 0.9$ with no further requirements. The count number is per 8 MeV.

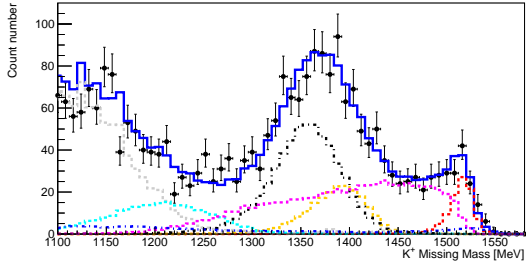
Appendix A Appendix



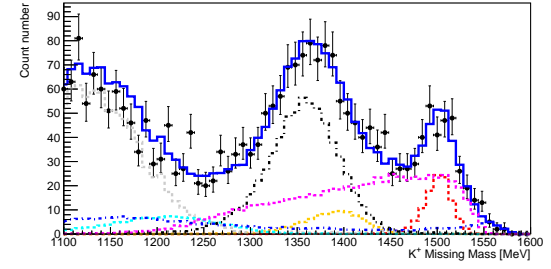
(a) Energy (1 610-1 665) MeV



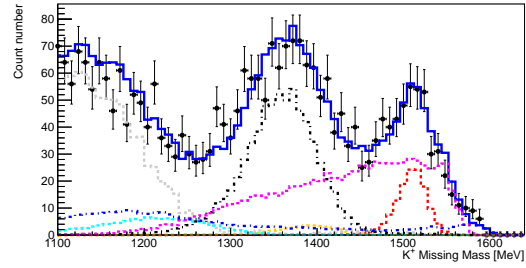
(b) Energy (1 665-1 719) MeV



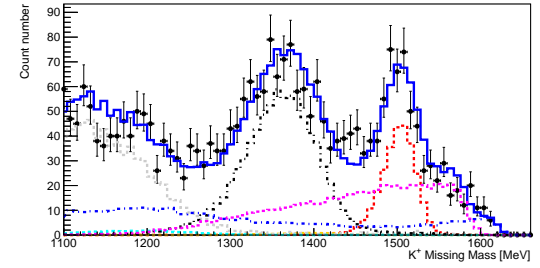
(c) Energy (1 719-1 773) MeV



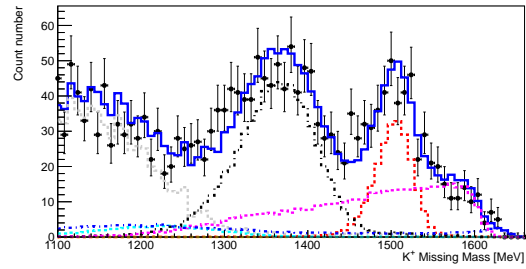
(d) Energy (1 773-1 828) MeV



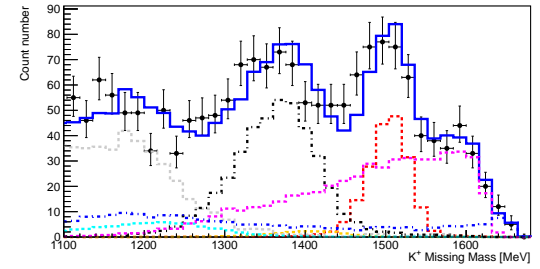
(e) Energy (1 828-1 882) MeV



(f) Energy (1 882-1 936) MeV



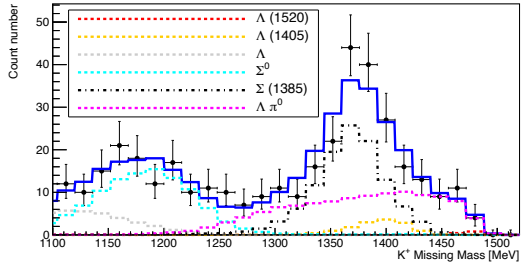
(g) Energy (1 936-1 979) MeV



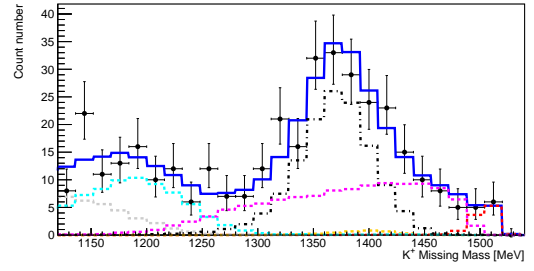
(h) Energy (1 979-2 015) MeV

Figure A.2: Fits to the missing mass to a K^+ at $\cos(\theta_{\text{CMS}}) > 0.9$ with additional π^0 required. The count number is per 8 MeV.

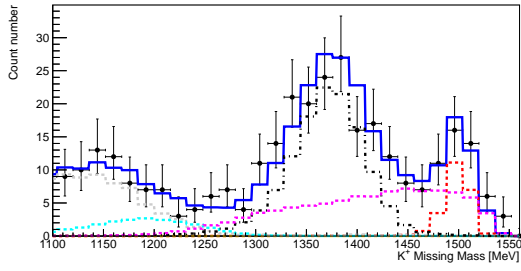
Appendix A Appendix



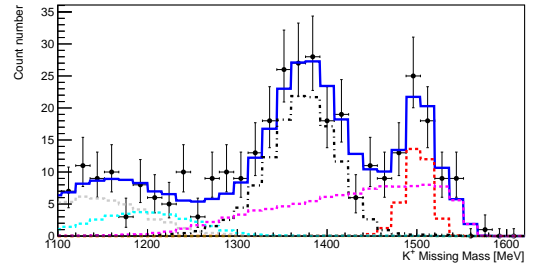
(a) Energy (1 610-1 665) MeV



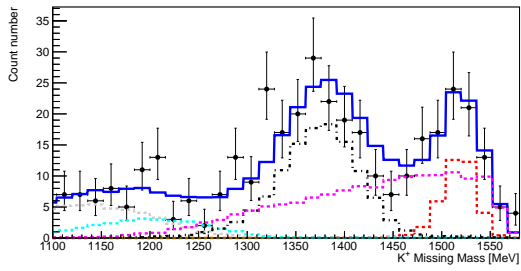
(b) Energy (1 665-1 719) MeV



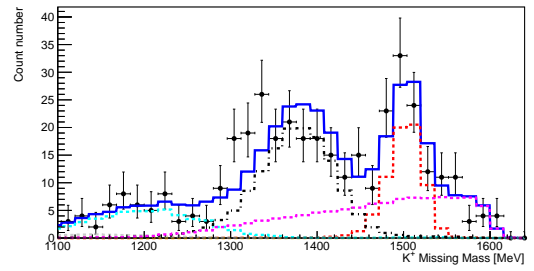
(c) Energy (1 719-1 773) MeV



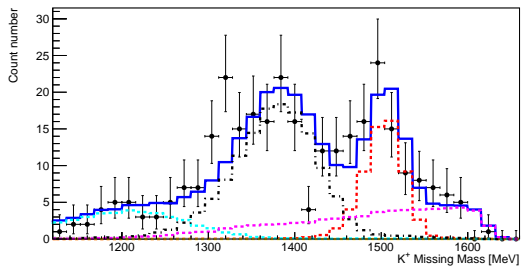
(d) Energy (1 773-1 828) MeV



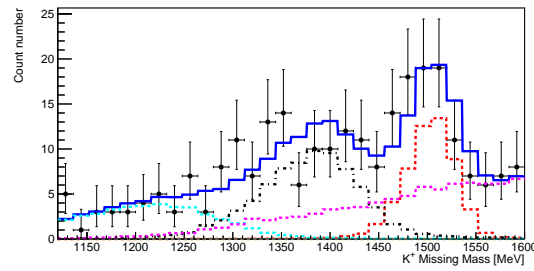
(e) Energy (1 828-1 882) MeV



(f) Energy (1 882-1 936) MeV



(g) Energy (1 936-1 979) MeV



(h) Energy (1 979-2 015) MeV

Figure A.3: Fits to the missing mass to a K^+ at $\cos(\theta_{\text{CMS}}) > 0.9$ with additional π^0 and γ required. The count number is per 16 MeV.

Bibliography

- [1] R. L. Workman et al., *Review of Particle Physics*, **PTEP** **2022** (2022) 083C01 (cit. on pp. 1–3, 19, 20, 23).
- [2] F.-K. Guo et al., *Hadronic molecules*, **Reviews of Modern Physics** **90** (2018), URL: <https://doi.org/10.1103/RevModPhys.90.015004> (cit. on pp. 1, 2).
- [3] S. Alef et al., *The BGOOD experimental setup at ELSA*, **The European Physical Journal A** **56** (2020) 104, URL: <https://doi.org/10.1140/epja/s10050-020-00107-x> (cit. on pp. 1, 4, 7).
- [4] H. Kohri et al., *Near-Threshold $\Lambda(1520)$ Production by the $\vec{\gamma} p \rightarrow K^+ \Lambda(1520)$ Reaction at Forward K^+ Angles*, **Phys. Rev. Lett.** **104** (17 2010) 172001, URL: <https://link.aps.org/doi/10.1103/PhysRevLett.104.172001> (cit. on pp. 1, 27, 28, 31).
- [5] B. Povh, K. Rith, C. Scholz and F. Zetsche, *Teilchen und Kerne. Eine Einführung in die physikalischen Konzepte*, Sixth, Springer-Verlag GmbH, 2004, ISBN: 3540210652 (cit. on pp. 2, 11).
- [6] M. Gell-Mann, *A schematic model of baryons and mesons*, **Physics Letters** **8** (1964) 214, ISSN: 0031-9163, URL: <https://www.sciencedirect.com/science/article/pii/S0031916364920013> (cit. on p. 2).
- [7] R. Aaij et al., *Observation of $J/\Psi p$ resonances consistent with pentaquark states in $\Lambda_b^0 \rightarrow J/\Psi K^- p$ decays*, **Physical Review Letters** **115** (2015), URL: <https://doi.org/10.1103/PhysRevLett.115.072001> (cit. on p. 2).
- [8] T. Hyodo, S. Sarkar, A. Hosaka and E. Oset, *Coupling of $\bar{K}^* N$ to the $\Lambda(1520)$* , **Phys. Rev. C** **73** (3 2006) 035209, URL: <https://link.aps.org/doi/10.1103/PhysRevC.73.035209> (cit. on p. 2).
- [9] MissMJ and Cush, *derivative work: Polluks - Standard Model of Elementary Particles.svg*, **Public Domain**, URL: <https://commons.wikimedia.org/w/index.php?curid=11307906> (cit. on p. 3).
- [10] Georg Scheluchin, *$\Lambda(1405)$ photoproduction with the BGO-OD experiment*, PhD thesis: Rheinische Friedrich-Wilhelms-Universität Bonn, 2020, URL: <https://hdl.handle.net/20.500.11811/8373> (cit. on pp. 5–8).

- [11] W. Hillert, *The Bonn Electron Stretcher Accelerator ELSA: Past and future*, *The European Physical Journal A - Hadrons and Nuclei* **28** (2006) 139, URL: <https://doi.org/10.1140/epja/i2006-09-015-4> (cit. on p. 5).
- [12] Hillert, Wolfgang et al., *Beam and spin dynamics in the fast ramping storage ring ELSA: Concepts and measures to increase beam energy, current and polarization*, *EPJ Web Conf.* **134** (2017) 05002, URL: <https://doi.org/10.1051/epjconf/201713405002> (cit. on p. 5).
- [13] *ELSA, Setup of ELSA*, URL: <https://www-elsa.physik.uni-bonn.de/elsa.html> (cit. on p. 6).
- [14] Oliver Freyermuth, *Studies of ω Photoproduction off Proton at the BGO-OD Experiment*, PhD thesis: Rheinische Friedrich-Wilhelms-Universität Bonn, 2017, URL: <https://hdl.handle.net/20.500.11811/7263> (cit. on p. 9).
- [15] *Homepage of Root*, 2022, URL: <https://root.cern> (cit. on p. 9).
- [16] S. Agostinelli et al., *Geant4—a simulation toolkit*, *Nuclear Instruments and Methods in Physics Research Section A: Accelerators, Spectrometers, Detectors and Associated Equipment* **506** (2003) 250, ISSN: 0168-9002, URL: <https://www.sciencedirect.com/science/article/pii/S0168900203013688> (cit. on p. 9).
- [17] E. Herlt and N. Salié, *Spezielle Relativitätstheorie*, Berlin, Boston: De Gruyter, 1978, ISBN: 9783112596067, URL: <https://doi.org/10.1515/9783112596067> (cit. on p. 10).
- [18] J. Olivero and R. Longbothum, *Empirical fits to the Voigt line width: A brief review*, *Journal of Quantitative Spectroscopy and Radiative Transfer* **17** (1977) 233, ISSN: 0022-4073, URL: <https://www.sciencedirect.com/science/article/pii/0022407377901613> (cit. on p. 13).
- [19] J. F. Kielkopf, *New approximation to the Voigt function with applications to spectral-line profile analysis*, *J. Opt. Soc. Am.* **63** (1973) 987, URL: <https://opg.optica.org/abstract.cfm?URI=josa-63-8-987> (cit. on p. 13).
- [20] D. P. Barber et al., *Strangeness Exchange in the Photoproduction of $K^+\Lambda(1520)$ Between 2.8-GeV and 4.8-GeV*, *Z. Phys. C* **7** (1980) 17 (cit. on p. 17).
- [21] U. Shrestha et al., *Differential cross sections for $\Lambda(1520)$ using photoproduction at CLAS*, *Phys. Rev. C* **103** (2 2021) 025206, URL: <https://link.aps.org/doi/10.1103/PhysRevC.103.025206> (cit. on p. 19).
- [22] W. Verkerke and D. P. Kirkby, *The RooFit toolkit for data modeling*, eConf **C0303241** (2003) MOLT007, ed. by L. Lyons and M. Karagoz, arXiv: [physics/0306116](https://arxiv.org/abs/physics/0306116) (cit. on p. 25).
- [23] S. Alef et al., *$K^+\Lambda$ photoproduction at forward angles and low momentum transfer*, *The European Physical Journal A* **57** (2021) 80, URL: <https://doi.org/10.1140/epja/s10050-021-00392-0> (cit. on p. 29).

List of Figures

2.1	Particles in the Standard Model of physics [9].	3
2.2	Decay scheme of the $\Lambda(1520)$. The decay channels with small branching ratios are left out. As the PDG does not state specific branching ratios for the different charges, all $\Sigma\pi$ -channels have the same value, which is the branching ratio for all three possibilities together. The branching ratios are taken from [1].	3
3.1	A three dimensional view on the <i>BGOOD</i> experiment. Picture taken from [3].	4
3.2	Overview of all detectors. The different detection mechanism are coloured. The illustration does not scale. The figure was taken from the PhD thesis of Georg Scheluchin [10, p. 17]	5
3.3	Setup of <i>ELSA</i> . Figure taken from [13].	6
3.4	Schematic setup of the photon tagger. Figure taken from [3, p. 12]	7
3.5	Side view of the <i>BGO Rugby Ball</i> . Figure taken from [3, p. 6].	7
3.6	Construction of a drift chamber. Figure taken from [14, p. 27]	9
4.1	Mass of particles in the forward spectrometer with momentum correction for K^+ and K^- respectively.	14
4.2	Fits to the mass of particles in the forward spectrometer (difference of positive and negative particles).	15
4.3	Cuts to the mass of particles in the forward spectrometer determined by the fits. The red and blue lines represent the FWHM and twice the FWHM respectively.	15
4.4	Invariant mass of two photons detected in the <i>BGO Rugby Ball</i> with fits and resulting mass ranges for selection.	16
5.1	Missing mass to K^+ and K^- , both detected in the forward spectrometer.	18
5.2	Missing mass to K^+ and p in the forward spectrometer.	18
5.3	The missing mass to proton and K^+ plotted against angle difference of charged particles in the <i>BGO Rugby Ball</i> and reconstructed K^-	19
5.4	Invariant mass of p detected in the forward spectrometer and π^0 detected in the <i>BGO Rugby Ball</i>	19
5.5	Missing mass to K^+ at $\cos(\theta_{K^+, \text{CMS}}) > 0.9$	21
5.6	Missing mass to K^+ after requiring an additional π^0 . Full possible range of E_γ	22
5.7	Missing mass to K^+ after two dimensional cut and additional π^0	22
5.8	Missing mass to K^+ and π^0 versus the missing mass to K^+ in case of simulated $\Lambda(1520)$ and $\Lambda(1405)$. Data was simulated for 100 million events each time.	23

List of Figures

5.9	Simulated data of the $\Lambda(1405)$, $\Lambda(1520)$ and $\Lambda(1670)$. Each time, 10 Million events were simulated. Missing mass to K^+ and π^0 plotted against the missing mass to K^+ . The horizontal line marks the mass of the Σ^0 and the diagonal line depicts the missing mass to K^+ minus the mass of a π^0 and thus a line, where the peak from other channels than $\Sigma^0\pi^0$ will approximately be.	23
5.10	Energy of the single photon in the <i>BGO Rugby Ball</i> boosted into the restframe of the reconstructed Σ^0 . The red lines represent the selection of the single photon.	24
5.11	Missing mass to K^+ after two dimensional cut and requirement of π^0 with additional photon.	24
5.12	The reconstruction efficiencies for the different requirements. Black triangles show the requirement of just a K^+ , red squares represent a K^+ with π^0 and the blue circles a K^+ with π^0 and γ	25
5.13	Photon flux.	26
5.14	Fit to the data with requiring just a K^+ at $\cos(\theta_{K^+, \text{CMS}}) > 0.9$ at beam energies (1 773-1 828) MeV.	27
5.15	Fit to the data with the other requirements at beam energies (1 773-1 828) MeV.	27
5.16	Differential cross section determined with the different requirements (as described in the legend). The data points are shifted by 2 MeV for better visibility. The black crosses are results from LEPS [4].	28
5.17	Differential cross sections for smaller angle bins. Only a K^+ is required. The numbers in the legend refer to the $\cos(\theta_{K^+, \text{CMS}})$. As a check of consistency the three small bins are averaged and compared to the result in figure 5.16 when requiring only a K^+ . The data points are slightly shifted for better visibility.	28
5.18	Estimation of the systematic error from selection of π^0 (and γ) and the fitting. The red line is the error weighted mean.	30
5.19	Estimation of the systematic error from selection of K^+ . The red line is the error weighted mean.	30
A.1	Fits to the missing mass to a K^+ at $\cos(\theta_{\text{CMS}}) > 0.9$ with no further requirements. The count number is per 8 MeV.	33
A.2	Fits to the missing mass to a K^+ at $\cos(\theta_{\text{CMS}}) > 0.9$ with additional π^0 required. The count number is per 8 MeV.	34
A.3	Fits to the missing mass to a K^+ at $\cos(\theta_{\text{CMS}}) > 0.9$ with additional π^0 and γ required. The count number is per 16 MeV.	35

List of Tables

- 4.1 Fit parameter for the K^+ shown in figure 4.2(a) and the proton shown in figure 4.2(b). . 14
- 5.1 Systematic errors in this analysis. The values apart from the last two are taken from [23]. 29